

Inelastic Neutron Scattering from MnF_2 in the Critical Region

Michael P. Schulhof*[†] and Robert Nathans*

Brookhaven National Laboratory, * Upton, New York 11973
and State University of New York at Stony Brook, New York 11790

and

Peter Heller[†]

Physics Department, Brandeis University, Waltham, Massachusetts 02154

and

Arthur Linz

Center for Materials Science and Engineering, Massachusetts Institute of Technology,
Cambridge, Massachusetts 02139

(Received 2 April 1971)

Detailed inelastic neutron-scattering measurements have yielded the behavior of both the transverse and longitudinal spin fluctuations throughout the critical region of the uniaxial antiferromagnet MnF_2 . The static susceptibilities, both transverse and longitudinal, are found to be adequately described by Ornstein-Zernike expressions, both above and below T_N , with κ_\perp remaining finite, while κ_\parallel approaches zero as T_N is approached from either side. Magnons are observed below T_N , the energy gap decreasing as $T \rightarrow T_N^-$ in a way which closely approximates the behavior of the sublattice magnetization. At a given $T < T_N$, the ratio of the magnon frequency to the magnon width decreases with increasing wave vector q . Above T_N , heavily damped magnonlike behavior is observed at large q , the peaks merging with decreasing q . The longitudinal fluctuation is always characterized by a single peak centered at $\omega=0$. Above T_N , the half-widths $\Gamma_\parallel(q, T)$ define a dynamical scaling function $\Omega_\parallel(q/\kappa_\parallel)$. In particular, the staggered ($q=0$) mode relaxation rate is approximately proportional to $T - T_N$ for $T > T_N$. However for $T < T_N$, Γ_\parallel appears to vanish as $q \rightarrow 0$ at all temperatures. Although the $T < T_N$ data for $\Gamma_\parallel(q, T)$ can also be described by a second scaling-function branch, the experimental accuracy and the range of q/κ_\parallel values spanned by the data at a given temperature are more restricted than above T_N . The behavior below T_N and at low wave vectors may possibly be associated with thermal diffusion within the spin system. At reduced temperatures below about 0.95, the numerical value of the observed longitudinal staggered susceptibility is consistent with the value calculated on the basis of the local energy-density fluctuations.

I. INTRODUCTION

Recently, it has become clear that a variety of physical systems exhibiting cooperative phenomena behave quite similarly in their respective critical regions.¹⁻³ With reference to a uniaxial antiferromagnet such as MnF_2 , some particularly interesting aspects of this behavior are (a) the vanishing of the sublattice magnetization as $T \rightarrow T_N^-$, (b) the anomaly in the longitudinal "staggered" susceptibility, (c) the anomaly in the longitudinal inverse correlation length κ_\parallel , and (d) the behavior of the relaxation rates $\Gamma(q)$, particularly for the longitudinal component of the spin fluctuation.

Of the theoretical ideas useful in describing critical behavior the concept of scaling⁴ has provided some of the most valuable insights. It now appears that scaling provides a very good description of the static behavior of a variety of systems.⁵ The further extension of the scaling hypothesis to dynamical behavior, as originally formulated by Ferrell *et al.*⁶ and extended and

applied to magnetic systems by Halperin and Hohenberg,⁷ has provided a framework for the interpretation of experimental data. Further theoretical advances have included the extension of dynamic scaling to anisotropic systems⁸ by Riedel and Wegner, and the detailed calculation of the scaling functions for isotropic ferro- and antiferromagnets by Résibois and Piette.⁹

The experimental measurement of the static wave-vector-dependent susceptibility in magnetic systems can usually be made by studying the angular dependence of the neutron scattering, i.e., in a "quasi-elastic" scattering experiment. Thus early work by Cooper and Nathans¹⁰ and Passel *et al.*¹¹ established the general static wave-vector-dependent behavior in ferro- and antiferromagnets. More recently, inelastic neutron scattering has been applied to the measurement of *dynamic* behavior. Thus Nathans, Menzinger, and Pickart¹² and Als-Nielsen *et al.*¹³ demonstrated the slowing of a critical mode as $T \rightarrow T_c^*$. Subsequent accurate measurements by Lau *et al.*¹⁴ established the va-

lidity of dynamical scaling^{7,9} above T_N in RbMnF_3 , an isotropic antiferromagnet. The ferromagnets iron¹⁵ and nickel¹⁶ have also been studied; a comparison¹⁷ with detailed theoretical predictions⁹ has been made for $T > T_c$.

In principle the behavior of the scattering function for any one Cartesian component of the spin fluctuation is obtainable via inelastic scattering. In practice, however, it was not possible in any of the previously mentioned studies to obtain separate information on the scattering functions for the longitudinal and transverse fluctuations below T_c . Thus, for example, in the work of Lau *et al.*¹⁴ on RbMnF_3 , the existence of a domain structure in the ordered state, and the nonexistence of an anisotropy gap, made it impossible to determine what part of the observed scattering arose from the longitudinal fluctuation and what part arose from the transverse. In fact, prior to the present work, separate measurements of even the static longitudinal and transverse susceptibilities had not been made for any magnetic system below T_c . In MnF_2 , a uniaxial antiferromagnet, the existence of a unique axis for the establishment of the staggered magnetization makes possible separate determinations of the longitudinal and transverse scattering behaviors throughout the critical region.

MnF_2 has been studied extensively by a variety of techniques including nuclear resonance,^{18,19} antiferromagnetic resonance,²⁰ specific heat,²¹ and ultrasonic attenuation.²² The present inelastic scattering work, a brief account of which appeared earlier,²³ follows our accurate measurement of the static aspects of the fluctuation behavior for $T > T_N$ using the quasi-elastic technique.²⁴ Earlier neutron-scattering work²⁵⁻²⁷ has largely concentrated on the behavior of the transverse fluctuations; these were studied more fully by Dietrich,²⁸ who obtained the q dependence of the magnon width at T_N , together with the decrease of the anisotropy gap below T_N . We have made an extensive study of the magnon frequency and width as a function of wave vector and temperature. We emphasize, however, that the transverse susceptibilities remain finite throughout the critical region. The transverse fluctuations thus never become critical in the sense of a diverging correlation range. Our primary interest was therefore in studying the dynamics of the *longitudinal* fluctuation. An aspect of this was to provide data for comparison with dynamical scaling theory in a weakly anisotropic system. Of particular interest, it turned out, was the behavior in the largely unexplored region below T_N .

The essential limitation in an experiment of this type is posed by the finite extent of the instrumental resolution function in the four-dimensional space of energy and momentum transfer.²⁹ To overcome

this problem it is necessary to be able to write the dependence of the observed neutron cross section in a theoretically reasonable form containing a number of parameters which are adjusted to obtain a best fit to the data. In Sec. II we discuss this form in detail, and describe the procedure for separating the effects of the longitudinal and transverse fluctuations. The neutron spectrometer, its resolution function, and other aspects of the experimental apparatus are described in Sec. III. In Sec. IV we present the detailed method of data analysis. The results of physical interest are given in Secs. V A and V B, respectively, for static properties and for dynamic properties. In Sec. V C we present an approximate analysis of the longitudinal relaxation behavior on the theory of dynamic scaling. The longitudinal relaxation behavior observed below T_N is discussed in Sec. VI with reference to recent quasihydrodynamic theories^{30,31} of the spin fluctuations in the ordered state. Section VII summarizes our main experimental findings.

II. ASSUMED FORM OF CROSS SECTION

The following is a presentation of the arguments leading to the adopted cross-section expressions, and enough theory to make possible an intercomparison of various aspects of the results. This enables us to check the entire body of data, including that of our quasi-elastic experiment, for internal consistency in as full a way as possible.

A. Separation of Transverse and Longitudinal Scattering

For a system of localized spins, each having the same magnetic form factor $F(\vec{K})$, the general formula³² connecting the magnetic-scattering cross section for unpolarized incident neutrons to the spin fluctuations may be written³³

$$\frac{d^2\sigma}{d\Omega d\omega} = \alpha \frac{K_f}{K_i} |F(K)|^2 \sum_{\alpha, \beta} (\delta_{\alpha\beta} - \hat{K}_\alpha \hat{K}_\beta) S^{\alpha\beta}(\vec{K}, \omega). \quad (1)$$

Here α is a constant, \vec{K}_i and \vec{K}_f denote, respectively, the incident and scattered neutron wave vectors, $\hbar\omega = \hbar^2(K_i^2 - K_f^2)/2m_0$ and $\hbar\vec{K} = \hbar(\vec{K}_i - \vec{K}_f)$ denote the neutron energy and momentum loss, respectively, the Greek letters α and β denote Cartesian components, and $\hat{K} = \vec{K}/|K|$. The scattering function $S^{\alpha\beta}(\vec{K}, \omega)$ is given by

$$S^{\alpha\beta}(\vec{K}, \omega) = (2\pi N)^{-1} \int_{-\infty}^{\infty} e^{-i\omega t} \langle S^\alpha(-\vec{K}, 0) S^\beta(\vec{K}, t) \rangle dt,$$

where

$$S^\alpha(\vec{K}, t) = \sum_n e^{i\vec{K} \cdot \vec{r}_n} S_n^\alpha(t), \quad (2)$$

the sum in (2) being extended over all N spins in

the sample. Here \vec{r}_n is the spacial location of the n th spin.

On account of its two-sublattice antiferromagnetic structure,³⁴ critical scattering in MnF_2 appears for \vec{K} near magnetic superlattice points $2\pi\vec{\tau}$ such that $e^{i2\pi\vec{\tau} \cdot (\vec{r}_n - \vec{r}_m)} = \pm 1$, the plus or minus signs holding for n and m belonging, respectively, to the same or to opposite sublattices. The set of reflections having this property includes the [100] and [001] reciprocal-lattice positions. For reasons that will be apparent shortly, we designate these positions, respectively, as $2\pi\vec{\tau}_M$ and $2\pi\vec{\tau}_P$. Thus

$$2\pi\vec{\tau}_M = (2\pi/a)\hat{a}; \quad 2\pi\vec{\tau}_P = (2\pi/c)\hat{c}.$$

Since $\exp[2\pi i(\vec{\tau}_M - \vec{\tau}_P) \cdot (\vec{r}_n - \vec{r}_m)] = +1$ independent of the sublattice assignments of spins n and m , we can write

$$S^{\alpha\beta}(2\pi\vec{\tau}_M + \vec{q}, \omega) = S^{\alpha\beta}(2\pi\vec{\tau}_P + \vec{q}, \omega) \equiv S^{\alpha\beta}(\vec{q}, \omega).$$

The separation of the effects of the longitudinal and transverse fluctuations, i.e., of the spin fluctuations, respectively, parallel or perpendicular to the [001] direction, may be accomplished as follows. Every measurement with \vec{K} near [100] is coupled with a measurement with \vec{K} near [001] as sketched in Fig. 1(a). Here \vec{K} is always in the (010) plane, and we have equal vector displacements \vec{q} from the two superlattice points. For the setting M , Eq. (1) then gives

$$\begin{aligned} \left(\frac{d^2\sigma}{d\Omega d\omega} \right)_M &= \alpha \frac{K_f}{K_i} |F(K)|^2 [S_{\parallel}(\vec{q}, \omega) + S_{\perp}(\vec{q}, \omega) - \epsilon_M(\vec{q}, \omega)], \end{aligned} \quad (3a)$$

while for the setting P we find

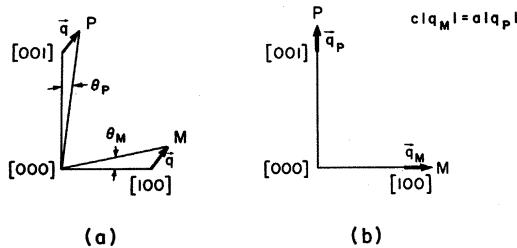


FIG. 1. \vec{K} -space settings for the measurement pairs used in the separation of the transverse and longitudinal scattering. In method (a) the vectorial displacements \vec{q} from the respective Bragg positions are the same. Method (b) takes advantage of the reduced wave-vector approximation. The displacement lengths have been exaggerated.

$$\left(\frac{d^2\sigma}{d\Omega d\omega} \right)_P = \alpha \frac{K_f}{K_i} |F(K)|^2 [2S_{\parallel}(\vec{q}, \omega) + \epsilon_P(\vec{q}, \omega)]. \quad (3b)$$

Here

$$\epsilon_{M,P}(\vec{q}, \omega) = \sin^2\theta_{M,P} [S_{\parallel}(\vec{q}, \omega) - S_{\perp}(\vec{q}, \omega)]. \quad (3c)$$

In writing (3) we have dropped the contributions from the terms in (1) with $\alpha = \beta$, since for a system with dominantly isotropic exchange interactions these terms should not contribute appreciably to the scattering.³³ Then, for this tetragonal system, the observed cross section will only depend on the transverse and longitudinal scattering functions, i.e., on the quantities

$$S_{\parallel}(\vec{q}, \omega) \equiv S^{\alpha\alpha}(\vec{q}, \omega) = S^{a'a'}(\vec{q}, \omega)$$

and

$$S_{\perp}(\vec{q}, \omega) \equiv S^{\alpha\alpha}(\vec{q}, \omega).$$

It is clear from (3) that these functions can be determined separately from such a pair of measurements.

In practice $\sin^2\theta_{M,P}$ was sufficiently small so that the terms $\epsilon_{M,P}(\vec{q}, \omega)$ could be neglected. Thus we can say that for \vec{K} near [001], the fluctuations in each of the two transverse directions contributed equally to the scattering, with no contribution from the longitudinal fluctuation. We called this the "pure transverse" reflection. For \vec{K} near [100], however, fluctuations in the longitudinal direction and in one of the transverse directions contributed equally. We called this the "mixed" reflection. The notational subscripts P ("pure") and M ("mixed") will now be clear.

B. Relation of $S_{\parallel}(\vec{K}, \omega)$ and $S_{\perp}(\vec{K}, \omega)$ to the Static Susceptibilities

The general relation of the scattering to the wave-vector-dependent static susceptibilities³⁵ $\chi(\vec{K})$ has been reviewed by Marshall and Lowde³³ and may be written

$$S_D^{\alpha\beta}(\vec{K}, \omega) = \chi^{\alpha\beta}(\vec{K}) F^{\alpha\beta}(\vec{K}, \omega) B(\omega, T) k_B T / g^2 \mu_B^2. \quad (4)$$

Here

$$B(\omega, T) = \hbar \omega \beta (1 - e^{-\hbar \omega \beta})^{-1},$$

with $\beta = (k_B T)^{-1}$, while S_D is the diffuse (non-Bragg) part of the scattering function, and $F^{\alpha\beta}(\omega)$ is a normalized spectral-shape function, i.e.,

$$\int_{-\infty}^{\infty} F^{\alpha\beta}(K, \omega) d\omega = 1. \quad (5)$$

More particularly, in systems like MnF_2 , where the magnetic ion lattice has reflection symmetry

about each point, $F^{\alpha\alpha}$ is real and even in ω . We assume in fact that $F^{\alpha\alpha}(\vec{K}, \omega)$ is a Lorentzian in ω centered about $\omega = 0$. Thus,

$$F^{\alpha\alpha}(\vec{K}, \omega) = \frac{1}{\pi} \frac{\Gamma_{\parallel}}{\omega^2 + \Gamma_{\parallel}^2}, \quad (6a)$$

where Γ_{\parallel} depends on both \vec{K} and T . For the transverse fluctuations where we have spin-wave behavior below T_N , we take

$$\begin{aligned} F^{\alpha\alpha}(\vec{K}, \omega) &= F^{\alpha'\alpha'}(\vec{K}, \omega) \\ &= \frac{1}{2\pi} \left[\frac{\Gamma_{\perp}}{\Gamma_{\perp}^2 + (\omega - \omega_0)^2} + \frac{\Gamma_{\perp}}{\Gamma_{\perp}^2 + (\omega + \omega_0)^2} \right], \end{aligned} \quad (6b)$$

where ω_0 and Γ_{\perp} depend on both \vec{K} and T . We assume that (6b) is also applicable above T_N , allowing ω_0 to be zero, if that fits the data best, which is the case at $q \approx 0$ above T_N . Using (4) and (6) we then have

$$S_{\parallel}(\vec{q}, \omega) = \frac{k_B T}{\pi g^2 \mu_B^2} B(\omega, T) \chi_{\parallel}(\vec{q}) \left[\frac{\Gamma_{\parallel}}{\Gamma_{\parallel}^2 + \omega^2} \right], \quad (7a)$$

$$\begin{aligned} S_{\perp}(\vec{q}, \omega) &= \frac{k_B T}{\pi g^2 \mu_B^2} B(\omega, T) \chi_{\perp}(\vec{q}) \\ &\times \frac{1}{2} \left[\frac{\Gamma_{\perp}}{\Gamma_{\perp}^2 + (\omega - \omega_0)^2} + \frac{\Gamma_{\perp}}{\Gamma_{\perp}^2 + (\omega + \omega_0)^2} \right], \end{aligned} \quad (7b)$$

where $\chi_{\parallel} (= \chi^{\alpha\alpha})$ and $\chi_{\perp} (= \chi^{\alpha\alpha'})$ as well as Γ_{\parallel} , Γ_{\perp} , and ω_0 depend on both T and q .

C. Theory for the \vec{K} Dependence of the Static Susceptibilities

1. Ornstein-Zernike Form; Reduced-Wave-Vector Approximation

A theory for $\chi(\vec{K}, T)$ based on the mean-field approximation was given originally by Moriya.³⁶ (See also Ref. 33.) An essential characteristic of the mean-field result is that at each temperature the reciprocal of the \vec{K} -dependent susceptibility is linearly related to the Fourier transform $J(\vec{K})$ of the spatial distribution of exchange interactions. For our purposes this may be stated as follows. Consider the rutile structure³⁴ of MnF_2 , and assume, as may be shown²⁵ from a number of experiments,^{20, 25, 37} that the dominant interaction is the antiferromagnetic coupling J_2 between a given Mn^{2+} ion and each of its eight nearest neighbors along $\langle 111 \rangle$ directions. Adopting a model³³ in which the exchange interaction is slightly anisotropic we have

$$\chi_{\parallel, \perp}^{-1}(\vec{K}, T) = f_{\parallel, \perp}(T)$$

$$+ g_{\parallel, \perp}(T) \cos(\tfrac{1}{2}K_x a) \cos(\tfrac{1}{2}K_y a) \cos(\tfrac{1}{2}K_z c), \quad (8)$$

where x , y , and z are taken along a , a' , and c , respectively, with³⁴

$$a = 4.8734 \text{ \AA}, \quad c = 3.3103 \text{ \AA} \quad (9)$$

the lattice parameters. As the anisotropy is slight, it follows that for $T > T_N$,

$$g_{\parallel}/g_{\perp} \approx 1 \approx f_{\parallel}/f_{\perp}. \quad (10)$$

In mean-field theory the form (8) is valid both above and below T_N . The relation (10) holds only for $T > T_N$, however.

The four coefficients in (8), of course, turn out experimentally to have temperature dependences quite different from those predicted by mean-field theory. We believe, however, that (8) should still provide a rather good account of the *shape* of the $\chi_{\parallel, \perp}^{-1}(\vec{K})$ -vs- \vec{K} curves for $T > T_N$. This may be substantiated, for example, for the case of the corresponding Ising model with the aid of the second-order scattering approximant of Fisher and Burford³⁸ [their Eq. (11.2)]. There the breakdown of the linear relation between $\chi_{\parallel}^{-1}(\vec{K})$ and $J(\vec{K})$ is slight, being a reflection of the small but nonzero value of the critical index η . Thus, for example, at $T = T_N$, Eq. (8) gives $\chi_{\parallel}^{-1}(\vec{q}) \propto q^2$, while Fisher and Burford find $\chi_{\parallel}^{-1}(\vec{q}) \propto q^{2-\eta}$ with $\eta = 0.05$. As our inelastic scattering data do not permit us to discern such slight differences, we will adopt (8) for $T > T_N$ with the understanding that the temperature dependences of the coefficients should be dictated by the data.

For $\vec{K} = 2\pi\vec{\tau} + \vec{q}$, we have

$$\chi_{\parallel, \perp}^{-1}(\vec{q}) = f_{\parallel, \perp} - g_{\parallel, \perp} [1 - \tfrac{1}{8}(q_x^2 a^2 + q_y^2 a^2 + q_z^2 c^2)]$$

to lowest order³⁹ in q . This leads to the Ornstein-Zernike form

$$\chi_{\parallel, \perp}(T, \vec{q}) = A_{\parallel, \perp}(T) / [q_*^2 + \kappa_{\parallel, \perp}^2(T)], \quad (11)$$

where

$$A_{\parallel, \perp} = 8a^{-2} g_{\parallel, \perp}^{-1}, \quad (12a)$$

$$\kappa_{\parallel, \perp}^2 = 8a^{-2} (f_{\parallel, \perp} g_{\parallel, \perp}^{-1} - 1), \quad (12b)$$

and

$$q_* = [q_x^2 + q_y^2 + (c/a)^2 q_z^2]^{1/2}. \quad (13)$$

Thus we refer all measurements of κ to the a axis.

Note from (13) that contours of equal susceptibility about each superlattice point are ellipsoids of minor to major axis ratio $c/a = 0.68$. We will in fact assume that this principle extends to the dynamical behavior as well, i.e., we assume that

$$S_{\parallel, \perp}(\vec{q}, \omega) = S_{\parallel, \perp}(q_*, \omega) \quad (14)$$

for small q_* . The approximation (14), which we

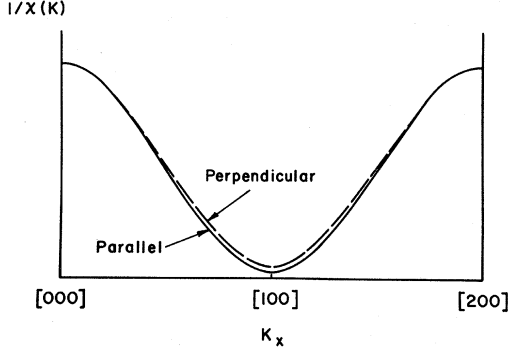


FIG. 2. Schematic behavior of the reciprocals of the \vec{K} -dependent transverse and longitudinal susceptibilities above T_N . The lower curve becomes tangent to the K_x axis as $T \rightarrow T_N$.

call the “reduced-wave-vector” approximation, makes possible a simplification in the technique for separating the longitudinal and transverse fluctuations: Again a measurement with \vec{K} near $2\pi\vec{\tau}_M$ is coupled with a measurement with \vec{K} near $2\pi\vec{\tau}_P$, but we now require only that the reduced-wave-vector displacements q_* be the same. For technical reasons to be discussed in Sec. IV A, the vectorial displacements were chosen parallel to the corresponding superlattice vectors, the settings for this method being as sketched in Fig. 1(b).

2. Relative Weight Factor $\lambda(T)$

Now consider the ratio of the slope of an Ornstein-Zernike plot for the longitudinal susceptibility to that for the transverse, i.e., the quantity

$$\lambda(T) = A_L(T)/A_T(T) . \quad (15)$$

For reasons discussed below we call this ratio the “relative weight factor.” It follows from (10) and (12a) that

$$\lambda \approx 1 , \quad (16)$$

at least for $T > T_N$. The fact that this is close to 1 will permit an important simplification in the data analysis.

We can provide another and perhaps more illuminating derivation of (16) as follows. Consider plots of $\chi_{||}^{-1}(\vec{K})$ and $\chi_{\perp}^{-1}(\vec{K})$ over an extended range of \vec{K} running from [000] to [200] as sketched in Fig. 2. This figure explicitly shows the experimental fact⁴⁰ that for a uniform field ($K=0$) the transverse and longitudinal susceptibilities are practically equal above T_N in MnF_2 . We see further that the two curves of reciprocal susceptibility are close to overlapping. This is a consequence of the weakness of anisotropic interactions relative to isotropic exchange interactions. Now from (11) and (15) we have that

$$\lambda = \left(\frac{d^2 \chi_{||}^{-1}}{dq_*^2} \right)_{q_*=0} \left(\frac{d^2 \chi_{\perp}^{-1}}{dq_*^2} \right)_{q_*=0}^{-1} , \quad (17)$$

the derivatives being evaluated at [100]. To the extent that the two curves in Fig. 2 are similar in shape, the ratio on the right in (17) should equal the ratio of the crest-to-trough heights of the two curves. Then

$$\lambda = \frac{1/\chi_{||}^{\text{unif}} - 1/\chi_{||}^{\text{stag}}}{1/\chi_{\perp}^{\text{unif}} - 1/\chi_{\perp}^{\text{stag}}} = \frac{\chi_{\perp}^{\text{unif}}}{\chi_{||}^{\text{unif}}} \left[\frac{1 - \chi_{||}^{\text{unif}}/\chi_{||}^{\text{stag}}}{1 - \chi_{\perp}^{\text{unif}}/\chi_{\perp}^{\text{stag}}} \right] , \quad (18)$$

where the superscripts unif and stag refer, respectively, to the cases $K=0$ and $q_*=0$. Note that the derivation of (18) did not depend on a particular shape (e.g., sinusoidal) for the two curves, but only on their having the same shape.

Using experimental data⁴⁰ for the uniform susceptibilities, and rough estimates of the ratios of the uniform and staggered susceptibility obtained from our data (see Sec. V A), we conclude from (18) that $\lambda = 1.01 \pm 0.05$ for $T > T_N$.

The situation below T_N is much less clear because the validity of the linear relation between $\chi^{-1}(\vec{K})$ and $J(\vec{K})$ is questionable there. Nonetheless we again employed (18), finding that λ increased gradually from 1.0 at T_N to 1.2 at 59.6°K, our lowest experimental temperature below T_N .

In practice we analyzed all our data using the value $\lambda = 1.05$ obtained⁴¹ from mean-field theory,³⁶ and employed in the analysis of our quasi-elastic scattering experiment.²⁴ It is clear from the preceding discussion that the result $\lambda \approx 1$ for $T > T_N$ does not depend on any mean-field assumptions. In view of the uncertain theoretical situation below T_N , however, we decided to check our results experimentally without any assumptions for the value of λ . This is discussed in Sec. IV D.

3. Ratio of Uniform and Staggered Susceptibilities

Assuming that (8) is correct, and noting that $1/\chi_{||,1}^{\text{stag}} = f_{||,1} - g_{||,1}$ while $1/\chi_{||,1}^{\text{unif}} = f_{||,1} + g_{||,1}$, and using (12b), we find

$$1 = (\chi_{||,1}^{\text{unif}}/\chi_{||,1}^{\text{stag}})(1 + 16a^{-2}k_{||,1}^{-2}) . \quad (19)$$

A somewhat more involved relation (for χ_{\perp}) is obtained if the inverse susceptibility versus wave-vector relation of Fisher and Burford³⁸ is used. In practice, however, this does not differ very much from (19). For example, in the Fisher-Burford theory the right-hand side of (19) would have the values 1.04 and 1.15, respectively, at temperatures 1.0 and 0.04°K above T_N .

Note that while (19) depends on the sinusoidal shape of the inverse susceptibility vs wave-vector curves, the Ornstein-Zernike form (11) is more

generally valid. Indeed it is clear that $\chi_{n,l}^{-1}$ will have a minimum at a superlattice vector. Then (11) should describe the behavior there, provided that the staggered susceptibility is finite, and that the reduced-wave-vector approximation holds.

4. Effect of Couplings Other than J_2

In addition to the dominant coupling J_2 described above, one should consider the coupling J_1 of a given spin to each of the two nearest neighbors in the c direction, and the coupling J_3 to each of the two nearest neighbors in the a or in the a' directions. This is discussed in Ref. 25, where it is concluded that $J_2 = -1.76^\circ\text{K}$, $J_1 = +0.32^\circ\text{K}$, and $|J_3| < 0.05^\circ\text{K}$. Then $J(\vec{k})$ can be calculated and the discussion of Secs. II C 1–II C 3 above modified. On this basis contours of equal susceptibility should be ellipsoidal with minor-to-major-axis ratio $(c/a)(1+r_1)^{1/2}(1+r_3)^{-1/2}$, where $r_1 = J_1/J_2$ and $r_3 = J_3/J_2$. As this amounts to a change of less than 11%, the approximation (13) should suffice for our purposes. Dietrich,²⁸ who looked into this experimentally for the case of the transverse static susceptibility above T_N , was in fact unable to find a significant departure from (14), using (13) to define q_* .

Next consider the modification of (19). Suppose that in analyzing the data we still obtain κ through (11), defining q_* through (13) without modification. Then (for either the longitudinal or transverse case) Eq. (19) becomes

$$\chi^{\text{stag}}/\chi^{\text{unif}} = 1 + 16a^{-2}\kappa^{-2}(1-r_{1,3})^{-1}, \quad (20)$$

where r_1 or r_3 apply with \vec{q} along c or along a , respectively.

The theory given for the relative weight factor λ evidently requires modification if r_1 and r_3 are anisotropic. Indeed, as the argument leading to (18) shows, a modification will be needed if the relative amount of higher Fourier components changes upon going from $\chi_n^{-1}(\vec{k})$ to $\chi_l^{-1}(\vec{k})$. This is probably not an important effect.

D. Anisotropy Field and χ_l^{stag} below T_N

In Moriya's mean-field calculation,³⁶ χ_l^{stag} is

$$\left(\frac{d^2\sigma}{d\Omega d\omega}\right)_P = |F(K)|^2 B(\omega, T) \frac{K_f}{K_i} \frac{A_P}{\kappa_1^2 + q_*^2} \frac{1}{2} \left[\frac{\Gamma_1}{\Gamma_1^2 + (\omega - \omega_0)^2} + \frac{\Gamma_1}{\Gamma_1^2 + (\omega + \omega_0)^2} \right] \quad (26)$$

and

$$\left(\frac{d^2\sigma}{d\Omega d\omega}\right)_M = |F(K)|^2 B(\omega, T) \frac{K_f}{K_i} \left\{ \frac{A_M}{\kappa_n^2 + q_*^2} \frac{\Gamma_n}{\Gamma_n^2 + \omega^2} + \frac{\lambda A_M}{\kappa_1^2 + q_*^2} \frac{1}{2} \left[\frac{\Gamma_1}{\Gamma_1^2 + (\omega - \omega_0)^2} + \frac{\Gamma_1}{\Gamma_1^2 + (\omega + \omega_0)^2} \right] \right\}. \quad (27)$$

constant below T_N . This follows from the proportionality of the anisotropy field to the sublattice magnetization, which is physically reasonable in MnF_2 where the anisotropy is largely of dipolar origin.⁴² Moriya obtained

$$\chi_l^{\text{stag}}(0^\circ\text{K}) = C/T_A, \quad (21)$$

where

$$C = g^2 \mu_B^2 S(S+1)/3k_B$$

is the Curie constant, and $T_A = 1.36^\circ\text{K}$. This numerical result follows from the physically apparent relation

$$\chi_l^{\text{stag}}(0^\circ\text{K}) = M_0(0)/H_A(0), \quad (22)$$

when the value $M_0(0) = Sg\mu_B = 5\mu_B$ is used for the magnetic moment per ion at sublattice saturation,⁴³ together with the original value^{42,20} $H_A(0) = 8800$ G for the anisotropy field at 0°K . If instead we use the value $H_A(0) = 7800$ G stated by Foner,⁴⁴ we obtain $T_A = 1.20^\circ\text{K}$.

In our experiment we can obtain alternate information on the temperature dependence of χ_l^{stag} by studying the spin-wave gap $G(T) = \omega_0(q=0, T)$. Indeed, assuming for $T < T_N$ that

$$\chi_l^{\text{stag}}(T) = M_0(T)/H_A(T), \quad (23)$$

and using the Kittel formula^{45,20} for $G(T)$, taking H_E proportional to M_0 , and noting that $H_A \ll H_E$, we have

$$\frac{\chi_l^{\text{stag}}(T)}{\chi_l^{\text{stag}}(0)} = \left[\frac{M_0(T)/M_0(0)}{G(T)/G(0)} \right]^2. \quad (24)$$

We expect that (24) should hold adequately as long as T is reasonably well below T_N .

E. Adopted Cross-Section Expressions

Now combining Eqs. (3), (7), (11), and (15), and using the notation

$$A_P = 2A_l(\pi g^2 \mu_B^2)^{-1} \propto k_B T; \quad A_M = A_n(\pi g^2 \mu_B^2)^{-1} \propto k_B T \quad (25)$$

and neglecting $\epsilon_{M,P}$ in (3), we have

Equations (26) and (27) describe the diffuse scattering; in addition a Bragg peak should be added to (27) at $q_* = 0$. In these cross sections, the parameters Γ_{\parallel} , Γ_{\perp} , and ω_0 depend on both q_* and T , while A_M , A_P , κ_{\parallel} , and κ_{\perp} depend only on T . From (25) and (15) we have

$$A_P/\lambda A_M = 2 \quad (28)$$

The physical significance of λ is clear from (27). It represents the fraction of the scattering in the mixed reflection due to the transverse fluctuations at a q_* value large compared with both κ_{\perp} and κ_{\parallel} : hence the term "relative weight factor." The meaning of (28) is also clear: In the mixed reflection we see the effect (proportional to λA_M) of the transverse fluctuations in only one of the two a directions. In the pure transverse reflection, however, we see the effect (proportional to A_P) of transverse fluctuations in both a directions. Hence $A_P = 2\lambda A_M$, giving (28).

Finally, using (11) and (25) we can write the (relative) static susceptibilities as

$$\chi_{\parallel}(\vec{q}, T) \propto A_M (\kappa_{\parallel}^2 + q_*^2)^{-1} T^{-1} \quad (29a)$$

and

$$\chi_{\perp}(\vec{q}, T) \propto A_P (\kappa_{\perp}^2 + q_*^2)^{-1} T^{-1} \quad (29b)$$

III. EXPERIMENTAL APPARATUS

A. Sample Crystal and Temperature Control

The 6.5-cm³ single-crystal MnF₂ sample used in this work, and the temperature control and measurement system, were described in connection with our earlier quasi-elastic scattering experiment.²⁴ The critical temperature

$$T_N = (67.459 \pm 0.007)^\circ \text{K} \quad (30)$$

was also determined there.

B. Triple-Axis Neutron Spectrometer

All measurements reported here were made on a three-crystal neutron spectrometer at the Brookhaven High Flux Beam Reactor. This spectrometer (see Ref. 29, Fig. 1 for the layout) included a deformed germanium-single-crystal masked monochromator, and a flat pyrolytic-graphite analyzer. This analyzer had a reflectivity approximately 5 times higher than a germanium crystal for the incident neutron energies (6.6 or 13 meV) employed. This was a very important feature, as the scattering we wished to study was often low in intensity. Soller slit systems, with 20-min horizontal collimation, were used to define the neutron paths. The vertical divergence, as determined by the natural collimator heights, was measured to be 48 min (0.14 rad). The beam incident upon the sample was monitored with the aid of a UF₆ fission

counter. A BF₃ detector was used following the analyzer.

The spectrometer could be operated at constant q (scanning ω) or at constant ω (scanning q). The former mode was used in all the MnF₂ measurements. Both modes were used for checking the resolution function.

C. Instrumental Resolution; Experimental Checks

The instrumental resolution function $R(\vec{q}_0, \omega_0, \vec{q}, \omega)$, which defines the probability of observing a scattering process at \vec{q} and ω with a nominal instrumental setting of \vec{q}_0 and ω_0 , was calculated analytically from the theory given by Cooper and Nathans.²⁹ According to this,

$$R(\vec{q}_0, \omega_0, \vec{q}, \omega) = R_0 \exp \left(-\frac{1}{2} \sum_{k=1}^4 \sum_{l=1}^4 M_{kl} x_k x_l \right) \quad (31)$$

Here $(x_1, x_2, x_3) = \vec{q} - \vec{q}_0$ and $x_4 = \omega - \omega_0$, where the 1 direction is chosen parallel to $\vec{K}_0 = \vec{q}_0 + 2\pi\vec{\tau}$, with the 3 direction vertical. The prefactor R_0 and the matrix elements M_{kl} are calculable slowly varying functions of ω_0 and \vec{K}_0 which also depend on the incident energy and the parameters of the instrument. It follows from (31) that contours of constant probability in (\vec{q}, ω) space are ellipsoids centered at (\vec{q}_0, ω_0) .

These calculations were checked by scanning through the [100] magnetic Bragg peak, in energy and in each component of the momentum transfer. The resulting good agreement with (31) gave us confidence in the theoretically calculated resolution function. This was important, as no such check was possible near [001], where magnetic Bragg scattering was absent. Some additional checks were made using the nuclear scattering at [002].

A numerical feeling for our instrumental energy resolution at 6.6-meV incident energy and near [100] may be conveyed as follows. Suppose first that the spectrometer were used to study a sample for which incoherent (i.e., \vec{q} -independent) elastic scattering occurs. Then upon scanning ω_0 at constant \vec{q}_0 , the detector count rate should be a Gaussian function of ω_0 , peaked at $\omega_0 = 0$, and of full width at half-maximum $\delta E_{\text{incoh}} = 0.13$ meV. This was checked experimentally by observing the scattering from a vanadium sample. Next suppose that an ω_0 scan is made through an elastic Bragg peak at constant $\vec{q}_0 = 0$. Then a Gaussian peaked at $\omega_0 = 0$ and of full width at half-maximum $\delta E_{\text{Bragg}} = 0.016$ meV is seen. In practice, a measure of the energy resolution will lie somewhere between the two numbers just quoted.

Now suppose we make an ω_0 scan through an elastic Bragg peak at a small constant $\vec{q}_0 \neq 0$. Then the count-rate maximum is found to occur at a

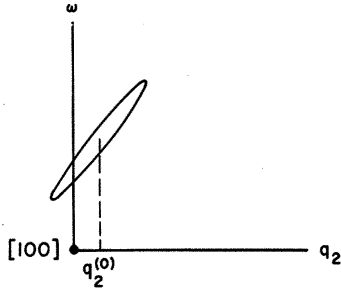


FIG. 3. Intersection of the resolution ellipsoid with the (ω, q_2) plane (schematic).

nonzero value of ω_0 . For $\vec{q}_0 = (0, q_2^{(0)}, 0)$, this maximum occurred for $\hbar\omega_0 = M_E^{(2)} q_2^{(0)}$, where $M_E^{(2)} = 6.4 \text{ meV \AA}$. This shift arises from the fact²⁹ that the intersection of the resolution ellipsoid with the $(\omega, q_2^{(0)})$ plane is a tilted ellipse as shown in Fig. 3. It is clear that for $\vec{q}_0 \neq 0$, an ω_0 scan past the Bragg peak gives a shifted maximum count rate. This effect was checked experimentally. It provided unambiguous proof that the central line observed in the mixed reflection critical scattering below T_N was not due to the passage of the Bragg peak through the wings of the instrumental resolution.

With an incident neutron energy of 13 meV, the instrumental energy resolution was poorer ($\delta E_{\text{incoh}} = 0.4 \text{ meV}$; $\delta E_{\text{Bragg}} = 0.024 \text{ meV}$). The resolution⁴⁶ in \vec{q} was about the same, however, and the count rates were higher by a factor of roughly 5. Thus the 13-meV measurements were used primarily at large q , where the critical scattering was relatively weak, and where high resolution in energy was not required.

The observed count rate $I(\vec{q}_0, \omega_0)$ is the convolution of the intrinsic cross section with the instrumental resolution function, i.e.,

$$I(\vec{q}_0, \omega_0) = b + P(\omega_0) \int \frac{d^2\sigma}{d\Omega d\omega}(\vec{q}, \omega) \times R(\vec{q}_0, \omega_0, \vec{q}, \omega) d^3q d\omega \quad (32)$$

Here b is the background, and the factor $P(\omega_0)$ includes the ω_0 dependence of the analyzer reflectivity. We measured $P(\omega_0)$ by a method due to Corliss and Hastings⁴⁷: With the beam from the monochromator incident directly on the analyzer, the latter was set to the Bragg angle, and the ratio of the detector count rate to the monitor count rate determined. This was repeated at different wavelengths by repositioning the monochromator. The background was determined as follows. With $\vec{q}_0 = 0$, ω_0 was set to a large value, far from the region of appreciable critical scattering. Next, with $\omega_0 = 0$, \vec{q}_0 was similarly offset. In both cases the

same count rate b was observed. This showed that the contribution from spin-incoherent scattering was small.

IV. DATA ANALYSIS

A. Data-Taking Procedure; Data Samples

Measurements were made at a set of eleven different temperatures in a 16°K region centered on the critical point. In each run the energy transfer ω was scanned at a fixed wave vector \vec{q} . This was repeated at values of q_* ranging from 0 to 0.257 \AA^{-1} . Each such run taken with \vec{k} near $[100]$ was coupled with a run with \vec{k} near $[001]$ as discussed in Secs. II A and II C 1. Above T_N we employed the settings of Fig. 1(b), i.e., the displacements \vec{q} were chosen parallel to the corresponding superlattice vectors for both the "mixed" and "pure transverse" scans. This geometry gave the greatest freedom from asymmetry, between positive and negative values of ω , due to the focusing properties of the instrumental resolution function. Below T_N , however, we worried that perhaps the magnon frequency might vary slightly with the direction of \vec{q} at a constant value of q_* . Then the settings of Fig. 1(a) were used. In particular, \vec{q} was taken parallel to $[101]$. This latter choice was made in order to have roughly comparable focusing for both the energy-gain and energy-loss magnon peaks.

Incident neutron energies of 6.6 and 13 meV were used, the former value being restricted to the smaller q values, the latter to the larger. Some intermediate q values were studied with both energies, providing a measurement of how the instrument constant $P(0)R_0$ changed upon going from 13 to 6.6 meV.

Typical data taken around the $[001]$ or "pure transverse" position are shown in Fig. 4. These data are representative of the temperature regions below, at, and above T_N , respectively. The three lower energy scans are at $q_* = 0.0645 \text{ \AA}^{-1}$, the upper three at $q_* = 0.129 \text{ \AA}^{-1}$. (The intensity units here should not be compared directly, as some of these scans were taken at 6.6 and some at 13 meV.) Below T_N renormalized spin waves are seen, the separation and width of the magnon peaks increasing with increasing q . At T_N and at small q the separation (energy gap) apparently has collapsed to zero, but the large- q data clearly exhibit a two-peaked structure. Even several degrees above T_N , the flat-topped curves are indicative that a two-peaked function is required to provide a satisfactory fit to the data. The small- q data above T_N are well fitted by a single Lorentzian, as might be expected in the hydrodynamic regime.

The corresponding scans taken near the "mixed" or $[100]$ position are displayed in Fig. 5. Below T_N the spin waves are again evident, although now

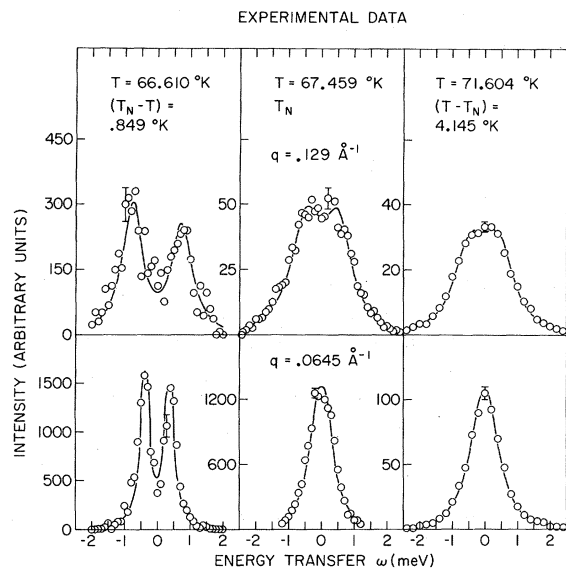


FIG. 4. Some energy scans near the [001] position at three different temperatures.

a central peak is unmistakably present. The fact that the intensity of this peak increased as $T \rightarrow T_N$ shows that it cannot be due to the passage of the Bragg peak through the wings of the instrumental resolution, confirming the conclusion reached earlier on the basis of the properties of the resolution function. (See Sec. III C.) Note that the transverse component in the mixed scan at $\omega = 0$ is never a sizable fraction of the total scattering there. This is comforting, since it is then not necessary to have a precise description of the transverse component in obtaining the longitudinal component by means of our subtraction procedure.

The solid lines in Figs. 4 and 5 are calculated by folding the cross-section expressions (26) and (27) with the instrumental resolution function. The excellent fits shown in these samples are typical of those generally obtained.

B. Possible Systematic Effects

Corrections for several possible systematic effects had to be looked into. These included background and spin-incoherent scattering, multiple Bragg scattering, extinction, instrumental misset, and magnetic Bragg-peak contamination of the critical scattering below T_N .

The background was determined by the method discussed in Sec. III C. It was not very dependent on the incident energy, being approximately 1 count/min at both 6.6 and 13 meV. The lack of any ω dependence at large q showed that the contribution from spin-incoherent scattering was small.

Multiple Bragg scattering can arise at relatively short incident wavelengths when several higher-

order reflections simultaneously satisfy the Bragg condition along with the reflection of interest, producing a small easily identified peak at the $\omega = 0$, $\vec{q} = 0$ position. This occurred in some of our $\vec{q} = 0$ scans, and was easily corrected for by deleting the single data point at $\omega = 0$.

Extinction due to Bragg scattering did not affect our critical scattering measurements as the sample was almost never close enough to the setting for a Bragg reflection to produce any attenuation of the incident beam. (Calculations show that at worst one point in a given energy scan might have been affected.) Extinction due to diffuse magnetic scattering—and in particular to the critical scattering itself—should also be considered as the Mn^{2+} cross section for paramagnetic scattering is not small, being about 21 b at long wavelengths.⁴⁸ At high temperatures this should lead to an attenuation of the incident beam by as much as 40% under the conditions of our experiment. However, detailed estimates show that the *change* in this attenuation produced either by changing the temperature or the sample orientation is probably a rather small fraction of the total attenuation and can be neglected in the analysis of the present data.

Instrumental settings were checked periodically during the work by instructing the computer to set the angles for a nuclear Bragg peak. It was possible to see errors of $\pm 0.01^\circ$, which is the limiting incremental angle for the spectrometer. The lattice-parameter values used in the computations were adjusted from the room-temperature values (9) with the aid of the thermal-expansion data of Gibbons.⁴⁹ In particular, $a(67^\circ\text{K})/a(300^\circ\text{K})$

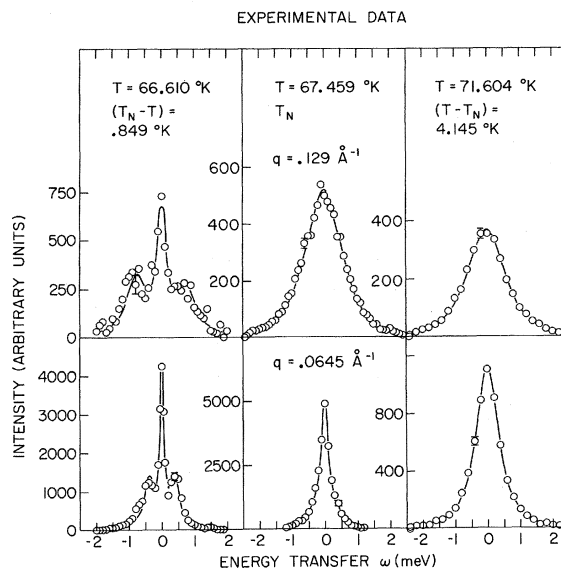


FIG. 5. Some energy scans near the [100] position at three different temperatures.

$= 1.00005$; $c(67^\circ\text{K})/c(300^\circ\text{K}) = 0.9987$. The effect of the thermal expansion over the critical region itself was not detectable.

For $q_* \geq 0.0257 \text{ \AA}^{-1}$ we can completely rule out the possibility of magnetic Bragg-peak contamination of the [100] critical scattering by the arguments of Secs. III C and IV A. Of course, the Bragg peak was absent from the [001] scattering even at $q = 0$.

C. Fitting Procedures

The cross-section expressions (26) and (27), folded with the resolution function using (32), were compared with the data as follows. For each energy scan, the goodness of fit was described by the weighted variance

$$\sigma^2 = (N - m)^{-1} \sum_{i=1}^N w_i (I_i^{\text{obs}} - I_i^{\text{calc}})^2. \quad (33)$$

Here N is the number of data points, m the number of free parameters, and

$$w_i = 1/I_i^{\text{obs}}$$

are the weighting factors appropriate to Poisson counting statistics. If the assumed cross section were correct we would have $\langle \sigma^2 \rangle = 1$ on account of the counting statistics. For optimum parameter values we obtained values of σ^2 between ≈ 1 and 3. This is statistically reasonable.

To perform the convolution integral (32) numerically we employed a grid of 10 000 points in (ω, \vec{q}) space, extending out to the contour $R/R_0 = 0.01$. To check convergence, the result was compared with the value obtained from a half-grid of 5000 points. If this produced a change of less than a few percent, the result was considered to represent the integral.

We now describe the fitting procedures in more detail.

1. Pure Transverse Data

In fitting to (26) above T_N , we fixed $\kappa_{\perp}(T)$ at the value determined in our quasi-elastic experiment.²⁴ Below T_N we took $\kappa_{\perp}(T) = (0.054 \pm 0.005) \text{ \AA}^{-1}$, the value found at T_N in the quasi-elastic work. The correctness of this choice was shown by the fact that a single normalization constant A_P fitted the data for all q at each $T < T_N$.

Since the parameters Γ_{\perp} and ω_0 depend on q , it was necessary to express their variation over the resolution volume with a reasonably accurate analytic form. The form chosen was a parabolic curve in q_* , i. e.,

$$\Gamma_{\perp}(\vec{q}) = a_{\perp} + b_{\perp} q_*^2, \quad \omega_0(\vec{q}) = a_0 + b_0 q_*^2. \quad (34)$$

The coefficients in (34) were determined by a fit to the data. Here we took advantage of the fact that the sensitivity of the fit to each coefficient depended

on the q region being investigated. For example, at small q the values of b_{\perp} and b_0 were relatively unimportant; the fitting program found values of a_{\perp} and a_0 which described the data best. (The values so obtained varied slightly with q .) Conversely at large q , a_{\perp} and a_0 were relatively unimportant and b_0 and b_{\perp} could be found. At intermediate q , a_{\perp} and a_0 were held fixed at the values previously determined, and b_0 and b_{\perp} were treated as adjustable. (The values so obtained varied somewhat with q .) Having determined all four coefficients at each experimental q , curves of $\Gamma_{\perp}(q_*)$ and $\omega_0(q_*)$ were constructed using (34). These showed that the initially used parabolic curves provided an adequate representation over the resolution volume.

2. Mixed Data

Having thus determined all the parameters appearing in the transverse contribution to (27) as a function of T and q , the data near [100] were fitted as follows. The relative weight factor λ was taken to be 1.05 as discussed in Sec. II C 2. Above T_N , $\kappa_{\parallel}(T)$ was initially set equal to the value found in the quasi-elastic work. This permitted the most accurate determination of the remaining parameters. The data were then reanalyzed treating κ_{\parallel} as adjustable. This second procedure, which was used for almost all the measurements below T_N , gave the κ_{\parallel} values denoted in Fig. 8 by the triangles. In this method we first guessed values of κ_{\parallel} for which the fitted normalization constant A_M came out essentially independent of q . Next, we used this κ_{\parallel} value, fitting at each q to A_M , and then constructing an Ornstein-Zernike plot of the quantity $A_M/(\kappa_{\parallel}^2 + q_*^2)$. Our values of κ_{\parallel} and $\chi_{\parallel}^{\text{stag}}$ below T_N are based on this latter method, which served as a useful internal check.

The procedure for handling the variation of Γ_{\parallel} over the resolution volume was similar to that described above for Γ_{\perp} and ω_0 . For example, consider the determination of the q dependence of Γ_{\parallel} at $T = T_N$. The initial assumption describing this was

$$\Gamma_{\parallel}(\vec{q}) = a_{\parallel} + b_{\parallel} q_*^2. \quad (35)$$

For each experimental q value, the coefficients a_{\parallel} and b_{\parallel} were determined by a fit to the data. (Here we were guided by the fact that the fit was relatively insensitive to a_{\parallel} at large q_* .) Then Γ_{\parallel} was computed at each q , and a curve of Γ_{\parallel} vs q_* was constructed. This curve was in fact found to be somewhat nonparabolic, being in better accord with a $\frac{3}{2}$ -power law. Next an expression of the form (35) was taken, but with the exponent 2 replaced by $\frac{3}{2}$. Then again a_{\parallel} and b_{\parallel} were determined for each experimental q value, and a second curve of Γ_{\parallel} vs q_* was constructed. In this case the coefficients a_{\parallel} and b_{\parallel} remained truly constant over the

entire set of q values (and in fact $a_{11}=0$). Furthermore, the second curve agreed with the first curve. Evidently, then, the initial parabolic trial function provided an adequate account of the variation in Γ_{11} over the resolution volume, and the results correctly describe the q dependence of Γ_{11} .

D. Checks on the Relative Weight Factor λ

Below T_N we were not sure of the correctness of the theory (Sec. II C 2) for the relative weight factor λ . We decided to look into this experimentally by taking advantage of Eq. (28), which expresses how the transverse component in a mixed scan compares with the corresponding pure transverse scan. This was done first above T_N , where we were confident that the result $\lambda \approx 1.0$ was correct. For our quasi-elastic data, taken at $T = 68.49^\circ\text{K}$ and at an incident energy of 77 meV, we found $A_P/1.05A_M = 2.05 \pm 0.15$. In other words, the transverse contribution to the [100] data was what one would expect on the basis of the [001] data, taking into account the known ratio of form factors and the fact that at [100] we see only one of the two Cartesian components of the transverse fluctuation. Alternatively, on requiring this to be the case, λ could be measured, and was indeed found to be close to unity. Now, still working at 68.49°K , but with an incident energy of 6.6 meV, our fitted values of A_M and A_P gave $A_P/1.05A_M = 1.72 \pm 0.17$. This is a 17% discrepancy somewhat outside of experimental error. A possible explanation of why this occurred at 6.6 and not at 77 meV is as follows. At 6.6 meV the neutron absorption in the sample is really quite high: An estimate based on the sample dimensions and the known cross sections for true absorption of manganese and fluorine showed that the over-all effect was to reduce the observed scattering by almost an order of magnitude. It follows that with our noncylindrical sample, the reduction factor might have changed appreciably upon rotating from the [001] to the [100] positions. This effect should be greatly reduced at 77 meV where the absorption is down by a factor of ≈ 5 . Another possible explanation is that there is some slight error in the calculation of how R_0 (the value of the resolution function at the ellipsoid center) changes in going from [100] to [001].

Since either mechanism should be temperature independent, some of the 6.6-meV data were re-analyzed by assuming that $A_P/\lambda A_M = 1.72$ also holds below T_N . First the [001] data were analyzed, yielding a value of A_P . Then the [100] data were fitted, treating A_M as a free parameter in the first term in (27), but taking the product λA_M in the second term to be $A_P/1.72$. This amounts to an absolute subtraction of the transverse component from

the mixed scan. The fit yielded a value of A_M , from which λ was computed by writing $\lambda = A_P/1.72A_M$. This gave $\lambda = 1.1 \pm 0.15$ at 66.61°K and $\lambda = 1.12 \pm 0.15$ at 59.55°K .

From this we conclude that the use of the value $\lambda = 1.05$ throughout the data analysis does not introduce significant error in the final results. Indeed we found that on varying λ by amounts considerably in excess of the limits just mentioned, the results were not affected to within the errors stated in Sec. V.

E. Accuracy of Parameter Determinations

The error limits quoted for each parameter, or for derived quantities, correspond to 1 standard deviation (67% confidence limits). These standard deviations were obtained from the size of the least-squares minimum in the fitting routine. They include the effect of correlation among the free parameters.

The stated errors do not include the uncertainty in our knowledge of the resolution function. We measured the resolution function with the ellipsoid centered near [100], and this agreed with calculations based on the theory of Cooper and Nathans²⁹ to within a few percent. Although this gives us some confidence in the calculated resolution function for other settings, we did not (and could not) make explicit measurements at such settings.

Finally, there remains the question of the accuracy of the assumed form of the cross section. This form together with the fitted parameter values always provided a very good representation of what we saw experimentally. Of course, we cannot guarantee uniqueness: There is never an absolute warranty that a different assumed form, with different parameter values, might not also represent the data equally well. Thus it is possible, in the region where resolution corrections are severe, that systematic errors in the assumed cross-section form can lead to systematic errors in the results of physical interest. This difficulty is inherent in the technique.

We can say, however, that the relatively simple assumed form, fitting as it did over a wide range of temperatures and wave vectors, consistently describes the results, and that numerous tests for internal consistency and continuity of the results were well satisfied.

V. RESULTS

In the remainder of this paper, including figures and tables, all wave-vector values refer to the quantity q_* defined in Eq. (13) and now referred to simply as q .

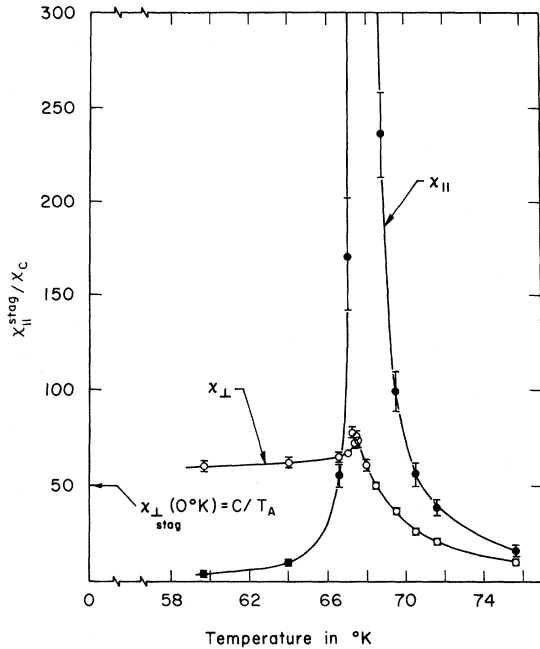


FIG. 6. Experimental results for the transverse (χ_{\perp}) and longitudinal ($\chi_{||}$) staggered susceptibilities plotted on the same scale. A theory for χ_{\perp} , together with experimental data for the anisotropy field, then permits a rough absolute calibration. The quantity $\chi_c = C/T_N$ is the susceptibility of an ideal Curie-law spin- $\frac{5}{2}$ paramagnet at $T = T_N = 67.46$ K.

A. Static Behavior

1. Staggered Susceptibilities; Rough Absolute Calibration

Relative values of the longitudinal and transverse staggered susceptibilities were obtained from (29) by setting $q = 0$, and are displayed in Fig. 6. The ratio $\chi_{||}^{\text{stag}}/\chi_{\perp}^{\text{stag}}$ was obtained above T_N in our quasi-elastic work.²⁴ For example, this ratio was 4.65 ± 0.9 at $T_N + 1$ K. (See Ref. 24, Fig. 2.) This allows us to put both curves of Fig. 6 on the same scale.

For reasons to be discussed in Sec. VI it is of interest to put these data on an absolute basis. Let $\chi_c = g^2 \mu_B^2 S(S+1)/3k_B T_N$ denote the susceptibility of an ideal Curie Law $S = \frac{5}{2}$ paramagnet at the MnF_2 critical temperature. We seek the quantity

$$C_{||} = \chi_{||}(T_N + 1 \text{ K})/\chi_c. \quad (36)$$

An approximate determination³⁰ of this calibration constant may be made in a number of ways as follows. In the first method, Eq. (24), together with our data for $G(T)$ (see below) and the NMR data¹⁸ for $M_0(T)/M_0(0)$, is used to estimate that $\chi_{\perp}^{\text{stag}}(59.6 \text{ K})/\chi_{\perp}^{\text{stag}}(0 \text{ K}) = 1.17 \pm 0.1$. Then Eq. (21) with $T_A = 1.36$ K may be used to establish the vertical scale in Fig. 6. This leads to $C_{||} = 225$

± 65 . If we use $T_A = 1.20$ K (see Sec. IID) we find $C_{||} = 255 \pm 75$. A second method of calibration relies on Eq. (19), together with data^{24,40} for $\kappa_{||}$ and $\chi_{||}^{\text{unif}}$. This gives $C_{||} = 260 \pm 35$. This assumes that the curves of Fig. 2 are sinusoidal. If instead we⁵⁰ employ (20), computing r_1 from the measured²⁵ exchange constants, we find $C_{||} = 220 \pm 35$. [The use³⁰ of the Fisher-Burford modification of (19) reduces these estimates by 4%.] Still a third calibration can be obtained by applying⁵⁰ (19) to the transverse susceptibility.⁵⁰ Using the data^{24,40} for κ_{\perp} and $\chi_{\perp}^{\text{unif}}$, together with the determination of $\chi_{||}^{\text{stag}}/\chi_{\perp}^{\text{stag}}$ discussed above, we find $C_{||} = 255 \pm 85$. On considering all these results we take

$$C_{||} \approx 240. \quad (37)$$

This is probably accurate to within $\pm 25\%$.

The anomaly in the longitudinal susceptibility is shown most clearly in Fig. 7, which includes the longitudinal data obtained in our quasi-elastic²⁴ work, normalized to the present data, and put on an absolute basis using (37). On fitting these data to $\chi_{||}(T) = b_+(T - T_N)^{-\gamma}$ for $T > T_N$ and $\chi_{||}(T) = b_-(T_N - T)^{-\gamma'}$ for $T < T_N$, we find

$$\gamma = 1.27 \pm 0.02, \quad (38a)$$

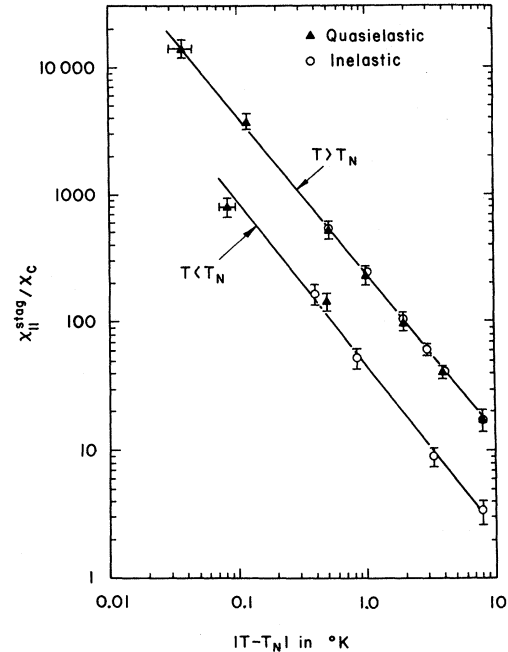


FIG. 7. Temperature dependence of the longitudinal staggered susceptibility above and below T_N . The scale of susceptibility has been chosen in accord with the approximate absolute calibration discussed in the text. Closed triangles denote the quasi-elastic measurements of Ref. 24. Open circles correspond to the present inelastic data.

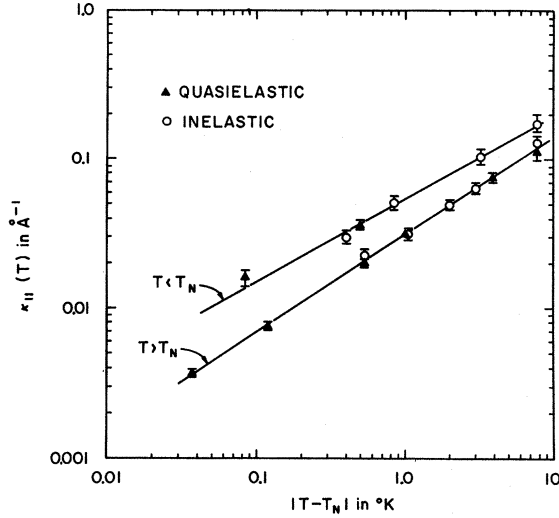


FIG. 8. Temperature dependence of the longitudinal inverse correlation length above and below T_N . Closed triangles denote quasi-elastic measurements of Ref. 24. Open circles correspond to the present inelastic data.

$$\gamma' = 1.32 \pm 0.06, \quad (38b)$$

and

$$b_+/b_- = 4.8 \pm 0.5. \quad (39)$$

The ratio in (39) is a good measure of what our data give for $\chi_{||}(T_N + |\Delta T|)/\chi_{||}(T_N - |\Delta T|)$. If we let $\chi_{||}(T)/\chi_c = C_+[(T - T_N)/T_N]^{-\gamma}$ for $T > T_N$, we find

$$C_+ = 1.15 \pm 0.3. \quad (40)$$

2. Inverse Correlation Lengths

The behavior of the longitudinal inverse correlation length $\kappa_{||}(T)$ is displayed in Fig. 8. These data include measurements (triangles) made using the quasi-elastic technique.²⁴ The consistency of the quasi-elastic and triple-axis results is good. On fitting to $\kappa_{||}(T) = \kappa_+(T - T_N)^\nu$ for $T > T_N$ and $\kappa_{||}(T) = \kappa_-(T_N - T)^{\nu'}$ for $T < T_N$ we find

$$\nu = 0.634 \pm 0.02, \quad (41a)$$

$$\nu' = 0.56 \pm 0.05, \quad (41b)$$

with

$$\kappa_+ = (0.032 \pm 0.004) \text{\AA}^{-1}, \quad (42a)$$

$$\kappa_- = (0.055 \pm 0.005) \text{\AA}^{-1}. \quad (42b)$$

Figure 8 shows that the ratio

$$\kappa_-/\kappa_+ = 1.7 \pm 0.3 \quad (43)$$

is a reasonably good average measure of $\kappa_{||}(T_N - |\Delta T|)/\kappa_{||}(T_N + |\Delta T|)$.

Our transverse data below T_N were in accord with a constant inverse correlation length $\kappa_\perp = (0.054$

$\pm 0.005) \text{\AA}^{-1}$, i.e., for this value a single normalization constant A_P fitted the data for all q at each temperature below T_N . The behavior of κ_\perp above T_N was described earlier.²⁴

3. Some Interpretive Discussion

The fact that $\chi_{||}^{\text{stag}}$ is roughly constant below T_N is a reflection of the approximate proportionality of the anisotropy field to the sublattice magnetization, as anticipated in Sec. IID. The situation above T_N has been described earlier.²⁴ In this connection we note that the fact that the curve-fitted divergence temperature²⁴ T_\perp came out such that $T_N - T_\perp > T_A \approx 1.3^\circ\text{K}$ can be understood qualitatively as follows. Imagine curves of $C/\chi_{||}^{\text{stag}}$ and $C/\chi_\perp^{\text{stag}}$ versus temperature drawn on the same plot for $T > T_N$. (Here C is the Curie constant.) Each curve will be straight with a unit slope at high temperatures, but will become concave-up in the critical region. From the results of Fig. 6, the ordinate of the upper (transverse) curve will be about $0.7T_A$ at T_N . This is, of course, where the lower-curve ordinate vanishes. Because of the curvature near T_N , the slope of the upper curve will be appreciably less than 1 there (e.g., it will be ≈ 0.4). It follows that T_\perp , which is the temperature at which the upper curve extrapolates to zero, will be such that $T_N - T_\perp$ is appreciably larger than $0.7T_A$. The result²⁴ $T_N - T_\perp \approx 2T_A$ is not surprising.

With regard to the behavior of $\chi_{||}^{\text{stag}}$ above T_N , the coefficient C_+ given in (40) is about 15% higher than the value⁵¹ stated for the BCC $S = \frac{1}{2}$ Ising model, and is thus consistent to within our large uncertainty. (In view of the difference in spin, it is not clear what this means, however.) Comparisons of our values of γ , ν , and κ_+ with Ising-model calculations have been given earlier.²⁴

The ratio $\chi_{||}(T_N + |\Delta T|)/\chi_{||}(T_N - |\Delta T|)$ can be obtained from the linear-model parametric-scaling-law equation of state of Schofield, Litster, and Ho.⁵² This theory requires $\gamma = \gamma'$. If we use $\gamma = 1.27$ and $\beta = \frac{1}{3}$ in Eq. (5) of Ref. 52, we find

$$\chi_{||}(T_N + |\Delta T|)/\chi_{||}(T_N - |\Delta T|) = 4.8, \quad (44)$$

in agreement with our finding (39).

It may be observed that this susceptibility ratio is apparently larger than the square of the κ ratio in (43). Similarly the discrepancy between γ' and $2\nu'$ appears to exceed that between γ and 2ν . [See Eqs. (38) and (41).] In view of the large experimental uncertainties, however, this requires a more careful investigation. This may be done as follows. According to (19), the ratios

$$R_{||,\perp} = (\chi_{||,\perp}^{\text{unif}}/\chi_{||,\perp}^{\text{stag}})(1 + 16a^{-2}\kappa_{||,\perp}^{-2}) \quad (45)$$

should be constant and equal to unity. Using the present results (together with quasi-elastic data

for κ_1 and χ_1), these ratios were computed for a number of temperatures throughout the critical region, and are displayed in Fig. 9. They do appear to be constant in the paramagnetic state. (This fact allowed us to make the absolute calibration by the second method, thus fixing $R_{\parallel} = 1$. The fact that $R_{\parallel} = R_{\perp}$ for $T > T_N$ led to the consistency of the second and third calibration methods.) Below T_N , however, R_{\parallel} seems to be departing appreciably from 1. This tendency is also exhibited, though less conclusively, by R_{\perp} .

The results of Fig. 9 may be interpreted as due to a change in shape of the χ^{-1} -vs- \vec{k} curves (Fig. 2) as T goes from above to below T_N . The fact that R_{\parallel} becomes greater than 1 is equivalent to the dip near $q=0$ becoming narrower and more rectangular below T_N .

B. Dynamic Behavior

1. Transverse Fluctuations: Magnon Frequencies

The dependence of the magnon frequency⁵³ parameter ω_0 upon temperature and wave vector over the entire range of our critical measurements is displayed in Fig. 10. (The uppermost curve is the 4.2 °K data of Ref. 25.) We thus see how the magnons "renormalize" with increasing T .

To provide an idea of the extent to which the magnon peaks represent well-defined propagating excitations, we have listed values of the ratios ω_0/Γ_1 for various values of q and T in Table I. This shows that at each temperature below T_N , the magnons are most sharply defined at small q . (A single exception to this rule occurred at 0.03 °K below T_N .) This is the situation expected theoretically for the isotropic antiferromagnet.³¹ The situation above T_N was quite the reverse. Here two magnonlike peaks were observed only at large

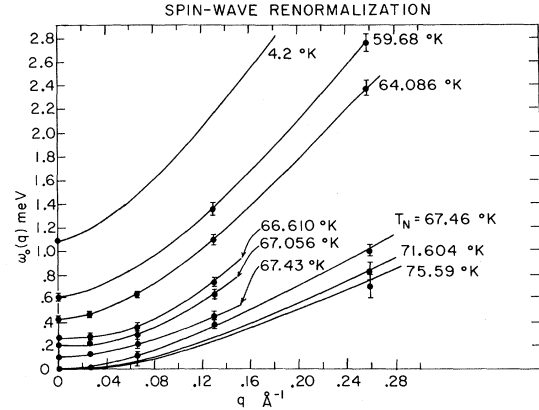


FIG. 10. Temperature and wave-vector dependence of the magnon frequency parameter ω_0 throughout the critical region. The extent to which the magnons are well-defined excitations is shown in Table I.

q . (See Fig. 4.) The ratios ω_0/Γ_1 become progressively smaller as q is decreased. This is reasonable physically: Above T_N it should only be possible to propagate spin-wave-like excitations within a region of correlated spins. Thus a propagating character can only be expected at large q .

Now consider the energy of the $q=0$ magnon, i.e., the gap $G(T)$. Our results for this are dis-

TABLE I. Ratio of magnon frequency to magnon width.

T (°K)	q (Å ⁻¹)	ω_0/Γ_1
59.68	0	24.6
	0.1289	11.9
	0.257	6.6
64.09	0	11.7
	0.0645	7.6
	0.1289	4.6
	0.257	3.0
66.61	0	3.7
	0.0645	2.5
	0.1289	2.2
67.06	0	2.3
	0.0645	1.7
	0.1289	1.7
67.35	0	1.0
	0.0645	0.95
67.43	0	0.82
	0.0645	1.15
67.46 = T_N	0	0
	0.0645	0.41
	0.1289	1.13
69.49	0	0
	0.0645	0.36
	0.1289	1.0
71.60	0	0
	0.0645	0.3
	0.1289	0.95
	0.257	0.9

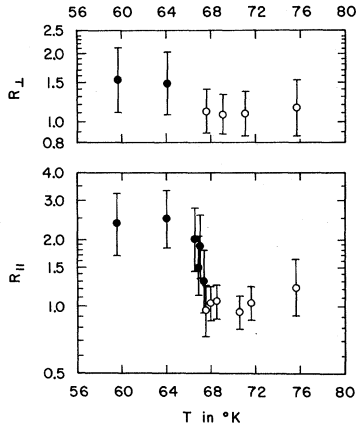


FIG. 9. Temperature dependences of the ratios R_{\parallel} and R_{\perp} defined in Eq. (45). Filled and open circles correspond, respectively, to $T < T_N$ and $T > T_N$.

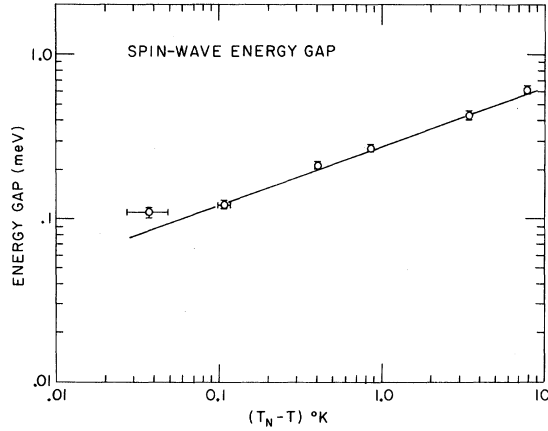


FIG. 11. Temperature dependence of the energy gap $G(T)$ below T_N .

played in Fig. 11. The solid line through the data points is a computer fit to a power law in $|\epsilon| = (T_N - T)/T_N$. We find

$$G(T) = (1.36 \pm 0.04 \text{ meV}) |\epsilon|^{0.37 \pm 0.02}. \quad (46)$$

Here T_N has been treated as a free parameter, giving $T_N = (67.47 \pm 0.03)^\circ\text{K}$, which is consistent with (30). [Alternatively if we fix T_N at the value given in (30), we obtain an exponent of 0.37 ± 0.01 .] We also measured the gap at 4.2°K , finding

$$G(4.2^\circ\text{K}) = (1.113 \pm 0.005) \text{ meV}. \quad (47)$$

This is very close to the result obtained by anti-ferromagnetic resonance,²⁰ namely, $(1.081 \pm 0.006) \text{ meV}$. As no significant change is expected between 4.2°K and $T=0$, we write (46) in the form

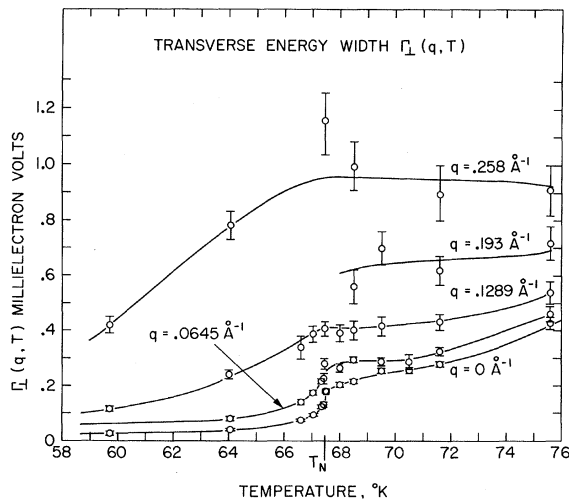


FIG. 12. Temperature and wave-vector dependence of the transverse relaxation rate throughout the critical region.

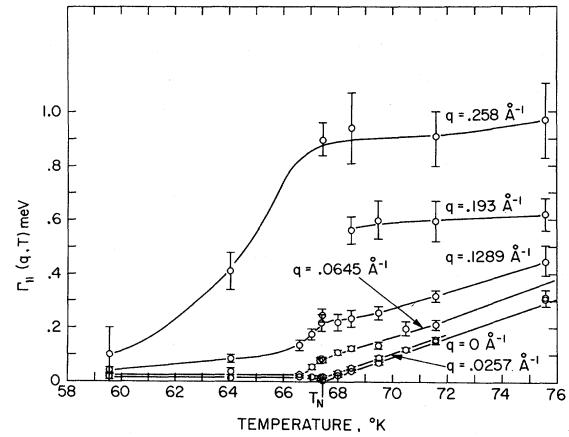


FIG. 13. Temperature and wave-vector dependence of the longitudinal relaxation rate throughout the critical region.

$$G(T)/G(0) = (1.20 \pm 0.06) |\epsilon|^{0.37 \pm 0.02} \quad (48)$$

for $0.1 < |\epsilon| < 0.0006$. This is quite similar to the behavior of the sublattice magnetization,¹⁸ namely,

$$M_0(T)/M_0(0) = (1.20 \pm 0.01) |\epsilon|^{0.333 \pm 0.005} \quad (49)$$

for $0.08 < |\epsilon| < 0.00007$. As discussed in Sec. II D, this similarity implies the approximate constancy of M_0/H_A and hence of χ_1^{stag} below T_N .

2. Transverse Fluctuations: Decay Rates Γ_\perp

The detailed behavior of the transverse relaxation rate (or magnon width) parameter $\Gamma_\perp(q, T)$ is displayed in Fig. 12. Note that for the staggered mode, Γ_\perp does not vanish at $T = T_N$, in contrast to the behavior of the corresponding longitudinal rate (see Fig. 13). We have in fact $\Gamma_\perp(0, T_N) = (0.18 \pm 0.01) \text{ meV}$. Below T_N , Γ_\perp becomes small at low q where we have well-defined magnons. At a fixed temperature (either above or below T_N), $\Gamma_\perp(q, T) - \Gamma_\perp(0, T)$ is roughly proportional to q^2 .

3. Longitudinal Decay Rates Γ_\parallel

Our results for the longitudinal relaxation rates $\Gamma_\parallel(q, T)$ are displayed graphically in Fig. 13. Since the data below T_N and at small q above T_N are not easily read from the graph, we have also listed them in Table II.

Above T_N the staggered mode relaxation rate $\Gamma_\parallel(0, T)$ appears to decrease roughly linearly in temperature, vanishing at T_N . This is shown in more detail in Fig. 14, where the solid line is a computer fit to a power law in $\epsilon = (T - T_N)/T_N$. This fit gives

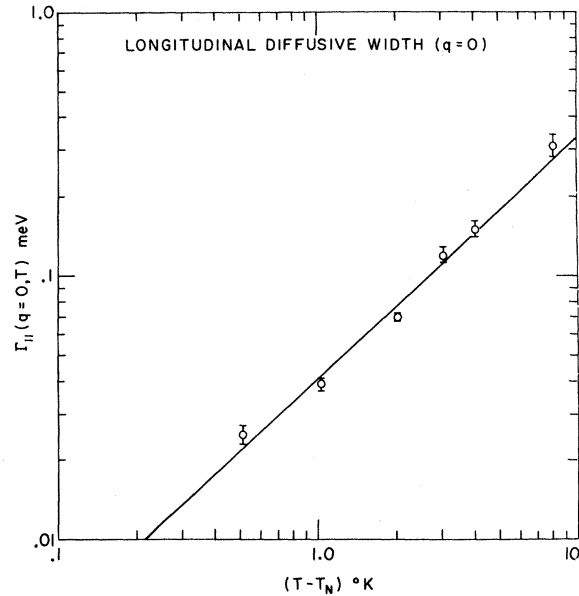
$$\Gamma_\parallel(0, T) = (2.1 \pm 0.1 \text{ meV}) \epsilon^{0.95 \pm 0.05}. \quad (50)$$

Riedel and Wegner⁸ have predicted that the anisotropy should produce a change in the power law

from an exponent (≈ 1) characteristic of the isotropic antiferromagnet to an exponent (≈ 1.3) close to T_N ; this crossover should occur where $\kappa_{\parallel} \approx \kappa_{\Delta} = \kappa_{\parallel}(T_N) = 0.054 \text{ \AA}^{-1}$, i.e., at $\approx 2^\circ\text{K}$ above T_N . Unfortunately on account of resolution limitations it was not possible to extend our measurements sufficiently close to T_N to obtain a direct check on this prediction. Our data are not inconsistent with the theory: Riedel⁵⁴ points out that with the exception of the point closest to T_N (which is 2 to 3 standard deviations high) the data of Fig. 14 are in accord with the detailed microscopic calculation⁸ of the crossover effect. The experimental difficulties being what they are, we also feel that the exponent in (50) should not be interpreted as showing that the behavior of MnF_2 is really that of an isotropic antiferromagnet. For simplicity, however, we will retain this exponent value in our dynamic scaling law analysis (Sec. VC). This is, of course,

TABLE II. Partial listing of $\Gamma_{\parallel}(q, T)$ data.

T ($^\circ\text{K}$)	q (\AA^{-1})	Γ_{\parallel} (meV)
59.55	0.0257	0.015 ± 0.01
	0.1289	0.041 ± 0.01
	0.258	0.10 ± 0.1
64.090	0.0257	0.009 ± 0.009
	0.0645	0.043 ± 0.015
	0.1289	0.086 ± 0.02
	0.258	0.408 ± 0.07
66.61	0.0257	0.017 ± 0.005
	0.0645	0.023 ± 0.007
	0.1289	0.135 ± 0.02
	0.257	0.017 ± 0.003
67.056	0.0645	0.052 ± 0.01
	0.1289	0.176 ± 0.02
	0.0257	0.021 ± 0.01
	0.0645	0.079 ± 0.01
67.430	0.0257	0.019 ± 0.005
	0.0645	0.075 ± 0.008
	0.1289	0.219 ± 0.03
	0	0.01 ± 0.005
67.70	0.0257	0.025 ± 0.01
	0.0645	0.093 ± 0.01
	0	0.025 ± 0.002
	0.0257	0.032 ± 0.003
67.982	0.0645	0.110 ± 0.008
	0	0.039 ± 0.002
	0.0257	0.048 ± 0.003
	0.0645	0.126 ± 0.008
68.495	0	0.0699 ± 0.004
	0.0257	0.088 ± 0.005
	0.0645	0.134 ± 0.013
	0	0.119 ± 0.01
70.517	0.0257	0.117 ± 0.01
	0.0645	0.199 ± 0.025
	0	0.150 ± 0.01
	0.0257	0.152 ± 0.01
71.604	0.0645	0.212 ± 0.02
	0	0.312 ± 0.03
	0.0645	0.302 ± 0.04
	0	

FIG. 14. Temperature dependence of the longitudinal staggered relaxation rate above T_N .

an approximation, but to go beyond this is really not justified by the data.

The q dependence of Γ_{\parallel} at T_N is shown in Fig. 15. The straight line corresponds to the power-law fit

$$\Gamma_{\parallel}(q, T_N) = (7.0 \pm 0.9 \text{ meV}) q^{1.6 \pm 0.2}. \quad (51)$$

Again it was not possible to take meaningful data

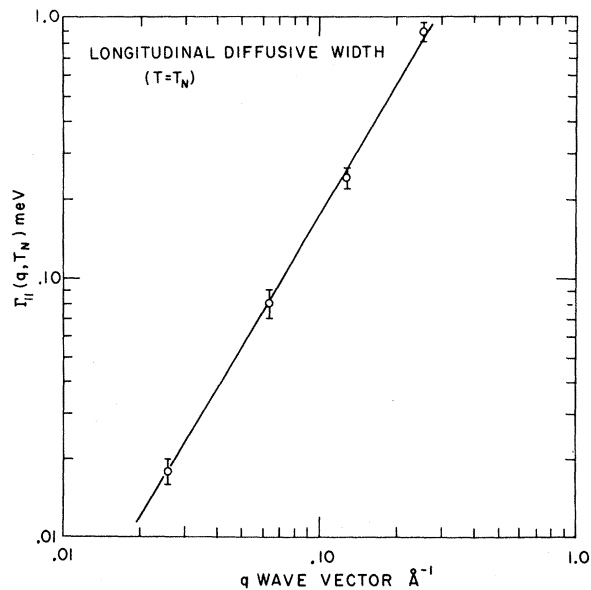


FIG. 15. Wave-vector dependence of the longitudinal relaxation rate at the critical temperature.

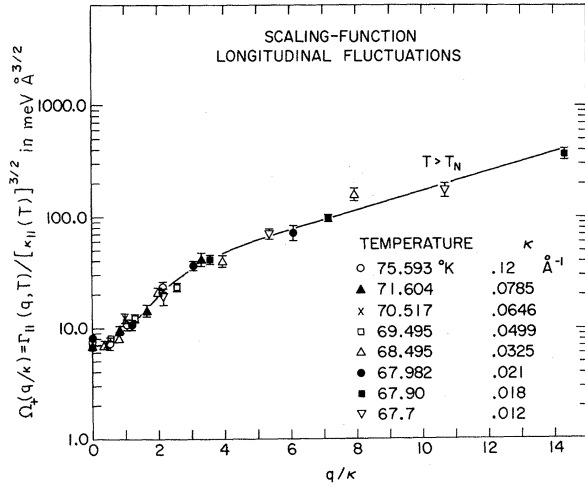


FIG. 16. Replot of the $T > T_N$ data of Fig. 13 in the form suggested by the dynamic-scaling theory. The ordinate is the scaled longitudinal relaxation rate; the abscissa is the scaled wave vector.

far enough into the region $q \ll \kappa_\Delta$ to obtain a direct check on the predicted⁸ exponent change. Riedel⁵⁴ has shown, however, that our data are consistent with the detailed microscopic calculation of the crossover. According to this, the slope of the data of Fig. 14 should really be intermediate between the values 2.0 and 1.5 appropriate to the regions $q \ll \kappa_\Delta$ and $q \gg \kappa_\Delta$, respectively.

C. Approximate-Scaling-Law Analysis of the $\Gamma_{||}(q, T)$ Data

Dynamic scaling predicts that the exponent expressing the dependence of $\Gamma_{||}(0, T)$ on $\kappa_{||}(T)$ above T_N should equal the exponent expressing the q dependence of $\Gamma_{||}$ at T_N . Using (50), (41a), and (42a) we find, for $T > T_N$,

$$\Gamma_{||}(0, T) = (6.6 \pm 0.6 \text{ meV}) [\kappa_{||}(T)]^{1.49 \pm 0.07} \quad (52)$$

when $\kappa_{||}$ is expressed in \AA^{-1} . The exponents in (51) and (52) do agree to within experimental error. They are consistent with the value $z = \frac{3}{2}$ expected theoretically⁷ for the isotropic antiferromagnet, although this may be due to our inability to take data close enough to the origin of the (κ, q) plane, as discussed in Sec. VB3. Pursuant to that discussion, however, we adopt the value $z = \frac{3}{2}$. We then interpret our data according to the general scaling prediction

$$\Gamma_{||}(q, T) = [\kappa_{||}(T)]^z \Omega_{\pm}[q/\kappa_{||}(T)], \quad (53)$$

with $z = \frac{3}{2}$.

At the outset of the present work, Hohenberg suggested that it might be possible to represent our data both above (+) and below (-) T_N in the

form (53), although the scaling function branches Ω_+ and Ω_- might have different behaviors for small values of the argument $x = q/\kappa_{||}$. Consider first the situation for $T > T_N$. In Fig. 16 we plot $\Gamma_{||}(q, T)/[\kappa_{||}(T)]^{3/2}$ against $q/\kappa_{||}(T)$. The points lie within 1 or 2 standard deviations of the drawn curve, with no systematic departures as a function of T and q . The scaling function $\Omega_+(x)$ thus defined may be fitted to a polynomial. For example, taking

$$\Omega_+(x) = A + Bx^2 + Cx^4 + Dx^6,$$

we find (in $\text{meV} \text{ \AA}^{3/2}$ units) $A = 6.95 \pm 0.2$, $B = 2.63 \pm 0.16$, $C = (-9 \pm 2) \times 10^{-3}$, and $D = (1.4 \pm 4.6) \times 10^{-5}$.

Now consider the data for $T < T_N$. Again we plot $\Gamma_{||}(q, T)/[\kappa_{||}(T)]^{3/2}$ against $q/\kappa_{||}(T)$. The results are displayed in Fig. 17. The data points scatter about a function (solid curve) which thus defines $\Omega_-(x)$. For large x , the behavior of $\Omega_-(x)$ merges with that of $\Omega_+(x)$ (dashed curve). This must be the case since our data at finite q are continuous at $T = T_N$. The behaviors of Ω_+ and Ω_- are very different at low values of x , however. The solid line corresponds to

$$\Omega_-(x) = 2.5 x^2 \quad \text{for } x \lesssim 2.$$

While this representation is a satisfying one, we would like to raise some cautionary notes. First, the data for $T < T_N$ are not very accurate. Thus for the Ω_- branch, the deviations about the "universal

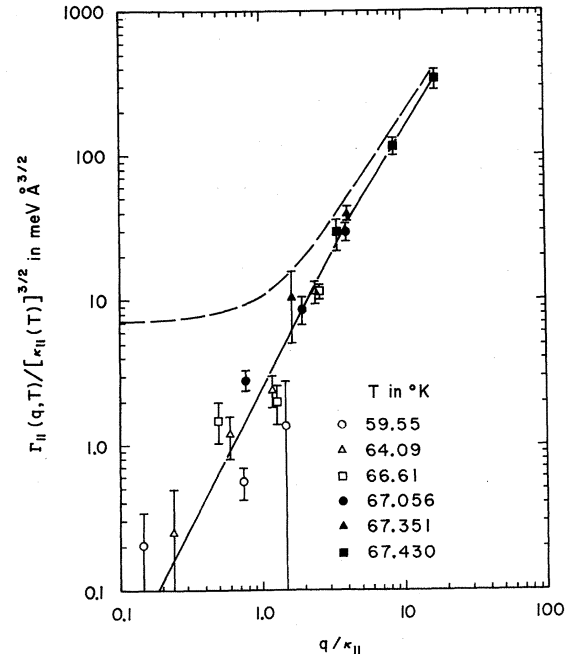


FIG. 17. Replot of the $T < T_N$ data of Fig. 13 in the form suggested by dynamical scaling. The dotted curve is taken from Fig. 16. Note the use of a logarithmic scale for the abscissa.

curve" (and the allowed errors, too) are quite large—a factor of 2 being not atypical. Second, for any one temperature below T_N , the range of $q/\kappa_{||}$ values spanned by the data is not large. For example, $q/\kappa_{||}$ ranged from 0.15 to 1.5 at 59.6°K, from 0.8 to 4 at 67.06°K, and from 4 to 17 at 67.43°K. Thus the "universal curve" is obtained in pieces. These do overlap to within the substantial errors mentioned above, forming a single curve which we can adopt as the scaling function $\Omega_*(x)$. Although it may be true, we cannot demonstrate that a continuation of any one of these pieces would really agree with the adopted curve.

The situation for the Ω_* branch is on a firmer footing. Here the accuracy of the data is higher (due to the larger linewidths). Also, the range of $q/\kappa_{||}$ values spanned by the data at any one temperature above T_N always includes the value ≈ 0 . The pieces of the universal curve thus always overlap at the left-hand end.

We can also carry out the scaling analysis for comparison with the theory of Résibois and Piette.⁹ For this purpose we can rewrite (53) for $T > T_N$ as

$$\Gamma_{||}(q, T)/\Gamma_{||}(q, T_N) = f(\kappa_{||}/q), \quad (54)$$

where $f(x) = Lx^\alpha \Omega_*(1/x)$ with $L \equiv \lim_{u \rightarrow \infty} u^\alpha/\Omega_*(u)$. In Fig. 18 we plot the left-hand side of (54) as ordinate with $\kappa_{||}/q$ as abscissa. This plot includes all our data for $T > T_N$ for which $q \neq 0$. The drawn solid line defining the scaling function f is evidently applicable with an accuracy of 1 or 2 standard deviations; there are no systematic departures a function of T or q . The dotted line is the scaling function calculated by Résibois and Piette⁹ for the isotropic antiferromagnet.

VI. DISCUSSION OF BEHAVIOR OF $\Gamma_{||}$ BELOW T_N

One of the most interesting aspects of the data

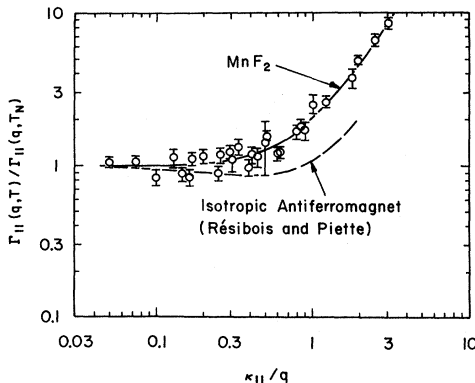


FIG. 18. Replot of the $T > T_N$ data of Fig. 13 in the form suggested by the dynamical-scaling representation of Résibois and Piette. The result of their calculation for the isotropic antiferromagnet is also shown.

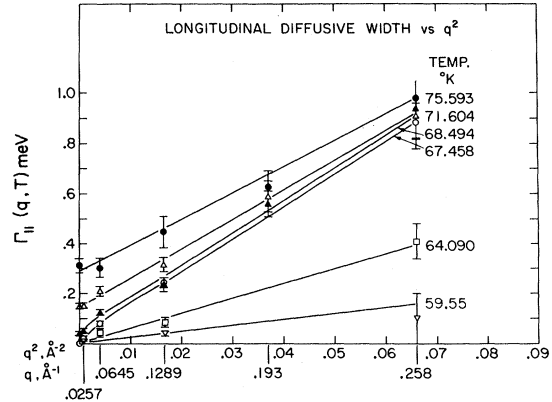


FIG. 19. Replot of the data of Fig. 13 in a way which best illustrates the change in longitudinal relaxation behavior upon going from the paramagnetic to the antiferromagnetic states.

is the behavior of the longitudinal relaxation rates for $T < T_N$. At the outset we expected the staggered mode rate to "slow down" as $T \rightarrow T_N^+$, and then "speed-up" again with decreasing T below T_N . The latter part of this prediction certainly was not fulfilled as Fig. 13 clearly shows. On the contrary, below T_N , $\Gamma_{||}$ appears to vanish as $q \rightarrow 0$ for all temperatures. To see this, and to see how the behavior above T_N merges with that below T_N , we have replotted the data of Fig. 13 in Fig. 19. Here the abscissa is q^2 and the temperature is a parameter. Well above T_N we find a roughly linear dependence on q^2 . Closer to T_N , the curves are apparently becoming steeper for low q , in keeping with the fact that at T_N a power law of degree $z < 2$ fits the data best. Below T_N the data for $\Gamma_{||}$ appear to extrapolate into zero as $q^2 \rightarrow 0$, although the data are not inconsistent with a small nonzero value. It is possible that a diffusion law $\Gamma_{||} = Dq^2$ applies at low q values, although the data by no means require this. The best one can say is that if such a law holds for our one or two lowest q values, then D is of the order of magnitude of $10 \text{ meV } \text{\AA}^2$ (or $\approx 10^{-3} \text{ cm}^2/\text{sec}$) at a few °K below T_N .

Theories pertaining to this behavior have been given by Halperin and Hohenberg^{31,55} and, independently, by one of us (P.H.).³⁰ A more detailed theoretical description has recently been provided by Huber,⁵⁶ using the hydrodynamics of Schwabl and Michel.⁵⁷ In these basically hydrodynamic theories, it is argued that a portion of the longitudinal scattering function should behave diffusively below T_N . This diffusivity is a manifestation of thermal diffusion taking place within the spin system. We may restate this as follows: Below T_N the local staggered magnetization is coupled to the local en-

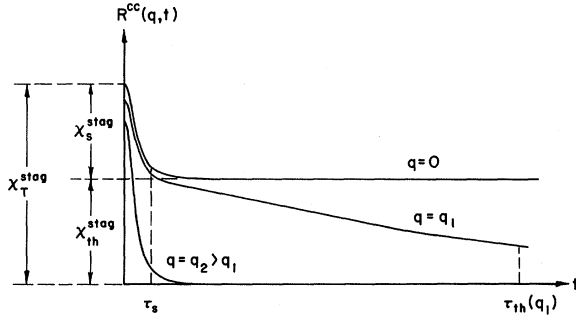


FIG. 20. Longitudinal relaxation behavior below T_N according to the quasihydrodynamic theories (Refs. 30, 31, 55, and 56). The uppermost curve corresponds to the relaxation that follows the turning-off of an exactly staggered field. The middle curve describes a case in which the applied field periodicity differs from that of the staggered mode by a small amount q_1 . The likely behavior at a larger value $q = q_2$ is sketched in the lowest curve.

ergy density. Fluctuations in the energy density then lead to a modulation of the intensity and sharpness of the magnetic Bragg peak, producing a surrounding halo of diffuse scattering.

In the approach taken in Ref. 30, the behavior is described in terms of the \vec{K} -dependent relaxation functions $R^{\alpha\beta}(\vec{K}, t)$. These functions are related essentially by Fourier transformation⁵⁸ to the non-Bragg part of the scattering function $S_D^{\alpha\beta}(\vec{K}, \omega)$, and may also be characterized as follows. Let the system be in equilibrium at temperature T in the presence of a field of spatial periodicity \vec{K} and small amplitude $H^\alpha(\vec{K})$ applied in the α direction. Let this field be turned off at time $t=0$. Let the average resulting spin-system response at wave vector \vec{K} and in direction β be written^{33,58}

$$\langle M^\beta(\vec{K}, t) \rangle = \langle M^\beta(\vec{K}) \rangle_{T, H=0} + H^\alpha(\vec{K}) R^{\alpha\beta}(\vec{K}, t). \quad (55)$$

Hence in particular

$$R^{\alpha\beta}(\vec{K}, 0) = \chi_T^{\alpha\beta}(\vec{K}). \quad (56)$$

The fact that the quantity on the right-hand side in (56) is the isothermal susceptibility has been emphasized with the subscript T .

For MnF_2 below T_N it is known experimentally⁵⁹ that the time-average staggered magnetic order persists over very large distances. Imagine that a field (directed along c and of wave vector \vec{K}_0 in exact spatial synchronism with this order) was turned off. If the spin system was thermally isolated, it would come to a new state of thermal equilibrium characterized by an altered value of the temperature. This is well known for the thermodynamics of ferromagnets as the "magnetocaloric effect." For our antiferromagnet, the temperature change will be

$$\delta T = -(T/C_H^*)(dM_0/dT) \delta H, \quad (57)$$

where δH and M_0 are, respectively, the field change and spontaneous average moment for an up-sublattice spin, and C_H^* is the magnetic specific heat per spin at zero staggered field. It follows from (55) and (57) that $R^{\alpha\beta}(\vec{K}_0, t)$ will have the form shown in the uppermost curve of Fig. 20. The initial drop is the adiabatic staggered susceptibility χ_s^{stag} . The constant value at large t is the quantity

$$\chi_{\text{th}}^{\text{stag}} = (T/C_H^*)(dM_0/dT)^2 = \chi_T^{\text{stag}} - \chi_s^{\text{stag}}, \quad (58)$$

which we call the "thermal part" of the staggered susceptibility. We note that a restoration of the temperature to the original value would produce a (up-sublattice) moment change $\chi_{\text{th}} \delta H$, thus allowing $R^{\alpha\beta}$ to drop to zero.

Now imagine that the periodicity of the applied field differed very slightly from that of the staggered mode, i.e., let \vec{q} be very small but not zero. There will now be a spatial beat frequency between the applied field and the spontaneous magnetization: The applied field will in some regions assist the spontaneous staggered magnetization and in other regions oppose it. Since the magnetocaloric expression (57) is linear in δH , the turning off of the field will lead, respectively, to temporary decreases and increases in the local value of the temperature. After a sufficient time, these regions will come into mutual thermal equilibrium, and the system will find itself at its initial temperature. The time constant τ_{th} for this process will be jointly proportional to the heat capacity of a region and to the thermal resistance between regions. Thus $\tau_{\text{th}} \propto (1/q)^2$. For the corresponding rate of decay $\Gamma_{\text{th}} = \tau_{\text{th}}^{-1}$ we then have

$$\Gamma_{\text{th}}(q, T) = D(T) q^2. \quad (59)$$

In fact, by the same calculation that leads to the Landau-Placzek result for a fluid we will have

$$D(T) = \Lambda / \rho C_H^*. \quad (60)$$

Here Λ is the thermal conductivity within the spin system and ρ is the number of spins per unit volume. Thus for a small but nonzero wave vector \vec{q}_1 , we are led to the relaxation function $R^{\alpha\beta}(\vec{q}_1, t)$ sketched in the middle curve of Fig. 20.

Of course, in order that we may justifiably talk in terms of a local time-varying temperature, equilibrium within each demagnetized region must be established quickly, i.e., we require that

$$\tau_s(T) \ll \tau_{\text{th}}(T, \vec{q}). \quad (61)$$

Here τ_s is the time constant for the exactly staggered mode relaxation. If τ_s is indeed finite, and if the thermal coupling to the lattice can be neglected, (61) should hold at small q . However, (61) no doubt fails at moderate q , where we surmise that

the over-all relaxation will no longer break up into two distinct parts. Indeed this is the case above T_N , and the shape of the relaxation function should vary continuously as we go around the critical point in the (κ, q) plane. Thus in the lowest curve of Fig. 20, we have depicted the relaxation function at a moderate wave vector q_2 by a single decay curve.

In drawing the bottom curve of Fig. 20, we have also assumed that the decay rate continues to increase with increasing q in this region. This is certainly reasonable, and has the following important consequence if we wish to use these theories for the interpretation of our MnF_2 data: It is quite possible that the experimentally observed increase of Γ_{\parallel} with increasing q took place entirely within the region $q \approx q_2$. In other words it is entirely possible that the breakup of the relaxation into two parts took place only for q smaller than the smallest experimental value (0.0257 \AA^{-1}). If this is true, then the apparent slope of the Γ_{\parallel} -vs- q^2 curve need not be related to the thermal diffusivity.

In view of the dynamical-scaling theory, one might be tempted to think that the crossover from the behavior of the middle to that of the lowest curve of Fig. 20 should occur for $q \approx \kappa_{\parallel}$. If this were true, and if scaling did indeed describe the thermal relaxation rate τ_{th}^{-1} for $q \ll \kappa_{\parallel}$, it would follow from (59), (60), and (53), with $\Omega_c(x) \propto x^2$, that $\Lambda/\rho C_H^* \propto (T_c - T)^{-2}$. However, there is theoretical⁶⁰ evidence that the energy fluctuation does not fit into the framework of dynamical scaling, and in particular that $\Lambda/\rho C_H^*$ is slowly varying with temperature (e.g., like $1/C_H$). There is therefore no reason to suppose that the condition $q < \kappa_{\parallel}$ would ensure the separated behavior of the middle curve.

An additional complication arises when we consider the possibility of energy exchange between the spin system and the lattice. This can clearly provide a nondiffusive decay process for the spin-system energy-density fluctuations.⁶¹ In this case a plot of Γ_{th} versus q^2 should effectively extrapolate into a value Γ_L characteristic of the spin-lattice interaction. [Of course, for q values corresponding to a truly macroscopic distance, such a plot will drop to zero with the very steep slope ($\approx 1 \text{ cm}^2/\text{sec}$) characteristic of the bulk thermal diffusivity,^{21, 62, 63} assuming macroscopically large antiferromagnetic domains.] These considerations also determine the behavior of the acoustic attenuation near the critical point.^{61, 64} From such data, from measurements of the anomalous change in the sound speed,⁶⁵ or from theoretical calculations,⁶⁶ it has recently been possible to obtain some information on the spin-lattice coupling. Thus, Huber⁶⁶ estimates $\Gamma_L \approx 10^7 \text{ sec}^{-1} \approx 10^{-5} \text{ meV}$, while an estimate by Kawasaki and Ikushima⁶⁵ (for $T > T_N + 0.2 \text{ }^\circ\text{K}$) gives $\Gamma_L \approx 3 \times 10^8 \text{ sec}^{-1} \approx 2 \times 10^{-4} \text{ meV}$. If

TABLE III. Observed versus calculated energy-fluctuation scattering below T_N .

T/T_N	$(\chi_{\parallel}^{\text{stag}}/\chi_c)_{\text{expt}}$	$(\chi_{\text{th}}^{\text{stag}}/\chi_c)_{\text{calc}}$
0.883	3.3 ± 1.3	2.9 ± 0.4
0.950	8.5 ± 3.5	7.8 ± 1.5
0.987	51 ± 20	39 ± 10
0.994	160 ± 70	93 ± 25

these estimates are applicable, the lattice involvement should not be very important at the experimental q values (see Table II).

For conditions where the middle curve of Fig. 20 provides a correct description of the relaxation function, the scattering function $S_{\parallel}(q, \omega)$ will consist of a narrow peak superimposed on a broad base. For small q the area of the narrow peak corresponds to $\chi_{\text{th}}^{\text{stag}}$; that of the broad base to χ_s^{stag} , while total area corresponds, of course, to χ_T^{stag} . It is then of interest to look into theories for the ratio $\chi_T^{\text{stag}}/\chi_{\text{th}}^{\text{stag}}$. On applying the linear-model parametric scaling-law equation of state,⁵² it may be estimated that³⁰ $\chi_T^{\text{stag}}/\chi_{\text{th}}^{\text{stag}} = 1.8 \pm 0.4$ in the critical region below T_N . In the Ising model computations of Baker and Gaunt,⁶⁷ $\chi_T/\chi_{\text{th}} < 1.1$ for reduced temperatures below 0.93, though this ratio increases as $T \rightarrow T_c$ to values consistent with the result of the linear model at the temperatures of interest to us. In any case, if τ_s^{-1} is large compared with both Γ_{th} and the experimental energy resolution, the narrow peak would dominate the observed scattering, and the experimentally deduced staggered susceptibility should equal $\chi_{\text{th}}^{\text{stag}}$. In other words the observed susceptibility should in this case correspond to the energy-density fluctuation.

We are then led to compare the numerical value of the longitudinal staggered susceptibility, obtained with the aid of the approximate absolute calibration discussed in Sec. V, with the value of $\chi_{\text{th}}^{\text{stag}}$ calculated from (62) using experimental data on the magnetic specific heat² and sublattice magnetization.^{18, 43} This comparison is presented in Table III. We see that for reduced temperatures below ≈ 0.95 , the observed and calculated susceptibilities are consistent. In other words the observed scattered intensity was consistent with the value expected on the basis of the energy-density fluctuations. Closer to the critical point, e.g., at $T/T_N \approx 0.99$, there is an indication that the observed scattering may exceed the energy fluctuation part by a numerical factor between 1 and 3. A possible interpretation of this latter result is as follows: Close to T_N , and for even the smallest experimental q values, either the description of the lowest curve of Fig. 20 is correct, or if the middle curve is applicable, both parts of the scattering

were lumped under the instrumental resolution function. Then the observed susceptibility was larger than χ_{th}^{stag} by a numerical factor $\approx \chi_T^{stag}/\chi_{th}^{stag}$. The observations are thus consistent with the above described theoretical values for this ratio.

It will, of course, be asked: Do the experimental data for the longitudinal scattering function exhibit a two-time-constant structure? The answer is that it is not possible to use the present data either to demonstrate this structure, or to contradict it. There are several technical reasons for this. The main difficulty is that the data for the longitudinal scattering were obtained essentially by subtracting the transverse scattering from the mixed [100] scattering. Since the transverse scattering is non-negligible, slight errors in the subtraction process may simulate the appearance of two time constants. Thus, while we do have some energy scans having this appearance, we cannot draw any reliable conclusions from them. Very close to T_N , where the subtraction effect is less severe, resolution effects are more serious, particularly if $1/\tau_S \rightarrow 0$ as $T \rightarrow T_N$.

While the hydrodynamic theories are helpful in understanding the numerical magnitude of the susceptibility, and in explaining the small and relatively temperature-independent values of $\Gamma_{||}$ observed at the lowest q values below T_N , other aspects of the data of Fig. 13 are not dealt with at all. Why, for example, does $\Gamma_{||}$ exhibit such a steep drop with decreasing temperature at large q values? The most important question, however, remains the following: Barring the involvement of the lattice in the thermal relaxation, it is surely reasonable to expect the description of the middle curve of Fig. 20 to be correct at sufficiently small q values. But how small is "sufficiently" small? In other words, where is the boundary of the hydrodynamic region of the (q, T) plane below T_N ?

VII. CONCLUSIONS

A detailed inelastic neutron scattering study has been made throughout the critical region of the uniaxial antiferromagnet MnF_2 . It was possible to separate the transverse and longitudinal scattering behaviors. The static susceptibilities, both longitudinal and transverse, were found to be adequately described by Ornstein-Zernike expressions both above and below T_N , with κ_{\perp} remaining nonzero and roughly constant below T_N , but with $\kappa_{||}$ approaching zero as T_N was approached from either side. Well below T_N , the numerical value of the observed

longitudinal staggered susceptibility is consistent with the value calculated on the basis of the energy-density fluctuations; closer to T_N it may exceed the calculated value by a numerical factor between 1 and 3.

The dynamics of the transverse fluctuation is as follows. Below T_N , the energy gap vanishes as $T \rightarrow T_N^-$ in a way which approximates the behavior of the sublattice magnetization, while the ratio of the magnon frequency to the magnon width decreases with increasing q . Above T_N heavily damped magnonlike behavior is observed at large q , the peaks merging at small q . The spectral width of the transverse fluctuations at a given wave vector increases monotonically with increasing temperature throughout the critical region.

The longitudinal relaxation behavior changes markedly in going from above to below T_N . The data above T_N define a scaling function $\Omega_+(q/\kappa_{||})$ to within the statistical errors of about 15%. The staggered-mode relaxation rate vanishes as $T \rightarrow T_N^+$, being roughly linear in $T - T_N$. Below T_N , however, $\Gamma_{||}^{stag}$ appears to vanish at all temperatures, the data for the q dependence of $\Gamma_{||}$ being consistent with, though by no means requiring, a diffusion law. These data may also be described by a second scaling-function branch Ω_- . However, in this case the experimental uncertainties are larger, and the range of $q/\kappa_{||}$ values spanned by the data at a given temperature is more restricted than for the data defining the Ω_+ branch.

It is possible that the behavior of the longitudinal relaxation rates below T_N and at low q is associated with thermal diffusion within the spin system. However, the extent and accuracy of the present data do not permit a determination of the true boundary of the hydrodynamic regime below T_N . Further work will be required to clarify the conditions under which it is possible to separate out the thermal part from the over-all longitudinal fluctuation as a function of wave vector and temperature. Further work is also needed to clarify the role played by the lattice.

ACKNOWLEDGMENTS

We gratefully acknowledge many fruitful discussions with Dr. M. Blume, Professor R. Ferrell, Professor R. B. Griffiths, Dr. P. C. Hohenberg, Professor D. Huber, Professor P. Martin, and Professor E. K. Riedel. Interest and advice were also generously given by Dr. L. Corliss, Dr. J. Hastings, and Dr. G. Shirane.

*Work performed under the auspices of the U.S. Atomic Energy Commission.

†Work supported by the U.S. Air Force Office of Scientific Research, Grant No. AF68-1480.

¹L. P. Kadanoff, W. Gotze, D. Hamblen, R. Hect, E.

A. S. Lewis, V. V. Palciuskas, M. Rayl, J. Swift, D. Aspnes, and J. Kane, *Rev. Mod. Phys.* **39**, 395 (1967).

²M. E. Fisher, *Rept. Progr. Phys.* **30**, 615 (1967).

³P. Heller, *Rept. Progr. Phys.* **30**, 806 (1967).

⁴B. Widom, *J. Chem. Phys.* **43**, 3898 (1965); L. P.

Kadanoff, *Physics* **2**, 263 (1966).

⁵See, for example, A. Arrott and J. E. Noakes, *Phys. Rev. Letters* **19**, 786 (1967); M. S. Green, M. Vicentini-Missoni, and J. M. H. Levelt-Sengers, *ibid.* **18**, 1113 (1967); J. T. Ho and J. D. Litster, *ibid.* **22**, 603 (1969); P. Schofield, J. D. Litster, and J. T. Ho, *ibid.* **23**, 1098 (1969).

⁶R. A. Ferrell, N. Menyhard, H. Schmidt, F. Schwabl, and P. Szeffalussy, *Phys. Rev. Letters* **18**, 891 (1967).

⁷B. I. Halperin and P. C. Hohenberg, *Phys. Rev.* **177**, 952 (1969).

⁸E. Riedel and F. Wegner, *Phys. Rev. Letters* **24**, 730 (1970); *Phys. Letters* **32A**, 273 (1970); see also T. Kawasaka, *Progr. Theoret. Phys. (Kyoto)* **41**, 1381 (1969).

⁹R. Résibois and C. Piette, *Phys. Rev. Letters* **24**, 514 (1970).

¹⁰M. J. Cooper and R. Nathans, *J. Appl. Phys.* **37**, 1041 (1966).

¹¹L. Passel, K. Blinowski, T. Brun, and P. Nielson, *Phys. Rev.* **139**, A1866 (1965).

¹²R. Nathans, F. Menzinger, and S. J. Pickart, *J. Appl. Phys.* **39**, 1237 (1968).

¹³J. Als-Nielsen, O. W. Dietrich, W. Marshall, and P. A. Lindgard, *J. Appl. Phys.* **39**, 1229 (1968).

¹⁴H. Y. Lau, L. M. Corliss, A. Delapalme, J. M. Hastings, R. Nathans, and A. Tucciarone, *Phys. Rev. Letters* **23**, 1225 (1969); *J. Appl. Phys.* **41**, 1384 (1970).

¹⁵M. F. Collins, V. J. Minkiewicz, R. Nathans, L. Passel, and G. Shirane, *Phys. Rev.* **179**, 417 (1969).

¹⁶V. J. Minkiewicz, M. F. Collins, R. Nathans, and G. Shirane, *Phys. Rev.* **182**, 624 (1969).

¹⁷J. Als-Nielsen, *Phys. Rev. Letters* **25**, 730 (1970).

¹⁸P. Heller, *Phys. Rev.* **146**, 403 (1966).

¹⁹P. Heller, in *Critical Phenomena*, edited by M. S. Green and J. V. Sengers, Natl. Bur. Std. Misc. Publ. No. 273 (U.S. GPO, Washington, D.C., 1966), p. 58.

²⁰F. Johnson and A. Nethercot, Jr., *Phys. Rev.* **114**, 705 (1959).

²¹D. T. Teaney, *Phys. Rev. Letters* **14**, 898 (1965).

²²Y. Shapira, S. Foner, and A. Missetich, *Phys. Rev. Letters* **23**, 98 (1969).

²³M. P. Schulhof, P. Heller, R. Nathans, and A. Linz, *Phys. Rev. Letters* **24**, 1184 (1970); See also P. Heller, M. P. Schulhof, R. Nathans, and A. Linz, *J. Appl. Phys.* **42**, 1258 (1971).

²⁴M. P. Schulhof, P. Heller, R. Nathans, and A. Linz, *Phys. Rev. B* **1**, 2304 (1970).

²⁵G. G. Low, A. Okazaki, R. W. H. Stevenson, and K. C. Turberfield, *J. Appl. Phys.* **35**, 998 (1964); A. Okazaki, K. C. Turberfield, and R. W. H. Stevenson, *Phys. Letters* **8**, 9 (1964).

²⁶K. C. Turberfield, A. Okazaki, and R. W. H. Stevenson, *Proc. Phys. Soc. (London)* **85**, 743 (1965).

²⁷B. H. Torrie, *Proc. Phys. Soc. (London)* **89**, 77 (1966).

²⁸O. W. Dietrich, *J. Phys. C* **2**, 2022 (1969).

²⁹M. J. Cooper and R. Nathans, *Acta Cryst.* **23**, 357 (1967).

³⁰P. Heller, *Intern. J. Magnetism* **1**, 53 (1970).

³¹B. I. Halperin and P. C. Hohenberg, *Phys. Rev.* **188**, 898 (1969).

³²L. Van Hove, *Phys. Rev.* **95**, 249 (1954); **95**, 1374 (1954).

³³W. Marshall and R. D. Lowde, *Rept. Progr. Phys.* **31**, 705 (1968).

³⁴R. A. Erickson, *Phys. Rev.* **90**, 779 (1953).

³⁵Following Ref. 33, the factor $|F(\vec{k})|^2$ is not included in these susceptibilities, which then have the periodicity of a lattice reciprocal to the lattice of magnetic spins. Physically $\chi(\vec{k})$ is then the spin-system response to a field which varies from ion to ion, but which is taken to be constant over the magnetization distribution within each ion. In our notation $\chi(\vec{k})$ is the response per ion, e.g., in the absence of exchange couplings we would have $\chi(\vec{k}, T) = \chi_0(T) = g^2 \mu_B^2 S(S+1)/3k_B T$.

³⁶T. Moriya, *Progr. Theoret. Phys. (Kyoto)* **28**, 371 (1962).

³⁷C. Trapp and J. W. Stout, *Phys. Rev. Letters* **10**, 157 (1963).

³⁸M. E. Fisher and R. J. Burford, *Phys. Rev.* **156**, 583 (1967).

³⁹This is adequate for our experimental wave-vector range $q < 0.258 \text{ \AA}^{-1} \approx 0.2(2\pi/a)$.

⁴⁰The anisotropy $\chi_{\parallel}^{\text{unif}} - \chi_{\perp}^{\text{unif}}$ was measured accurately by J. W. Stout and M. Griffel, *J. Chem. Phys.* **18**, 1455 (1950). For recent separate measurements of χ_{\parallel} and χ_{\perp} see S. Foner, in *Magnetism*, edited by G. T. Rado and H. Suhl (Academic, New York, 1963), Vol. I, p. 387. See also C. Trapp, thesis (University of Chicago, 1963) (unpublished).

⁴¹G. Parette and K. U. Deniz, *J. Appl. Phys.* **39**, 1232 (1968).

⁴²F. Keffer, *Phys. Rev.* **87**, 608 (1952); T. Oguchi, *ibid.* **111**, 1063 (1958).

⁴³A. M. Clogston, J. P. Gordon, V. Jaccarino, M. Peter, and L. R. Walker, *Phys. Rev.* **117**, 1222 (1960).

⁴⁴S. Foner, in *Magnetism*, edited by G. T. Rado and H. Suhl (Academic, New York, 1963), Vol. I, p. 387.

⁴⁵C. Kittel, *Phys. Rev.* **82**, 565 (1951).

⁴⁶Our q -space resolution near [100] was such that $M_{11} = 8.7 \times 10^4 \text{ \AA}^2$, $M_{22} = 9.9 \times 10^5 \text{ \AA}^2$, and $M_{33} = 1.5 \times 10^3 \text{ \AA}^2$ at 6.6 meV, while at 13 meV, $M_{11} = 5.6 \times 10^4 \text{ \AA}^2$, $M_{22} = 8.9 \times 10^5 \text{ \AA}^2$, and $M_{33} = 8.5 \times 10^2 \text{ \AA}^2$. Thus, for example, in a scan of $q^{(0)}$ past an elastic Bragg peak a width full-width at half-maximum (FWHM) of 0.0025 \AA^{-1} is observed. The resolution in other directions was less good.

⁴⁷L. M. Corliss and J. Hastings (private communication).

⁴⁸G. E. Bacon, *Neutron Diffraction* (Oxford U.P., Oxford, England, 1962), p. 149.

⁴⁹D. F. Gibbons, *Phys. Rev.* **115**, 1194 (1959).

⁵⁰The determination of κ_{\parallel} in Ref. 24 is based primarily on the mixed [100] scattering data for which $\vec{q} \parallel c$, since a crystal angle scan was employed. Then $r_1 \approx -0.18$ should be used in (20). In the determination of κ_{\perp} , we had $\vec{q} \parallel a$. Then $r_3 \approx 0$ should be used.

⁵¹See Ref. 2, Table 2.

⁵²P. Schofield, J. D. Litster, and J. T. Ho, *Phys. Rev. Letters* **22**, 603 (1969).

⁵³A brief account of this has been given, in Proceedings of the International Conference on Magnetism, Grenoble, France, 1970, *J. Phys.* (to be published).

⁵⁴E. K. Riedel, *J. Appl. Phys.* **42**, 1383 (1971).

⁵⁵See also P. C. Hohenberg, *Varena Summer School Lectures on Critical Phenomena*, 1970, pp. 82-88 (unpublished).

⁵⁶D. Huber, *Intern. J. Quantum Chem.* (to be published).

⁵⁷F. Schwabl and K. H. Michel, *Phys. Rev. B* **2**, 189 (1970) (ferromagnets); K. H. Michel and F. Schwabl, *Z. Physik* (to be published) (antiferromagnets).

⁵⁸See Ref. 33, Eqs. (43), (48), and (69). Note that

$\hbar\omega\beta(1 - e^{-\hbar\omega\beta})^{-1} = 1$ for our data, and that we have incorporated the factor $g^2\mu_B^2N^{-1}$ into our definition of R .

⁵⁹H. A. Alperin, P. J. Brown, R. Nathans, and S. J. Pickart, Phys. Rev. Letters **8**, 237 (1962).

⁶⁰K. Kawasaki, Progr. Theoret. Phys. (Kyoto) **40**, 706 (1968).

⁶¹K. Kawasaki, Phys. Letters **29A**, 406 (1969).

⁶²G. A. Slack, Phys. Rev. **122**, 1451 (1961).

⁶³J. W. Stout and E. Catalano, J. Chem. Phys. **23**, 2013 (1955).

⁶⁴B. Luthi and R. J. Pollina, Phys. Rev. Letters **22**, 717 (1969); G. Gorodetsky, B. Luthi, and T. J. Moran, in *Proceedings of Conference on the Dynamic Aspects of Critical Phenomena* (Fordham U. P., New York, 1970).

⁶⁵K. Kawasaki and A. Ikushima, Phys. Rev. B **1**, 3143 (1970).

⁶⁶D. Huber, Phys. Rev. B **3**, 805 (1971).

⁶⁷G. A. Baker, Jr. and D. S. Gaunt, Phys. Rev. **155**, 545 (1967).

Magnetomechanical Ratios for Ferrites with Composition $\text{Zn}_x\text{M}_{1-x}\text{Fe}_2\text{O}_4$

G. G. Scott and R. A. Reck

Research Laboratories, General Motors Corporation, Warren, Michigan 48090

(Received 5 April 1971)

Magnetomechanical ratios have been measured for 21 different ferrites having the compositional formula $\text{Zn}_x\text{M}_{1-x}\text{Fe}_2\text{O}_4$. Room-temperature g' values were determined for four different series where $M = \text{Mg}^{2+}$, Ni^{2+} , Fe^{2+} , and $(0.5 \text{ Li}^+, 0.5 \text{ Fe}^{3+})$, and g' values near the Néel temperature were determined for $M = \text{Ni}^{2+}$, $x = 0.73$.

INTRODUCTION

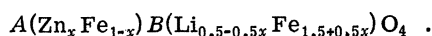
Magnetomechanical ratios (g') have been determined by the Einstein-de Haas method for 21 different ferrites fitting the compositional formula $\text{Zn}_x\text{M}_{1-x}\text{Fe}_2\text{O}_4$, where M is Mg^{2+} , Ni^{2+} , Fe^{2+} , or $(0.5 \text{ Li}^+, 0.5 \text{ Fe}^{3+})$. Details of the experiments and a discussion of errors are given in earlier papers.^{1,2}

The samples used for all of these determinations were made by the usual powder sintering process and furnace cooled. They were then accurately ground to cylinders having a diameter of 0.561 in. and a length of about 0.75 in. These short cylinders were placed in a hollow pendulum¹ producing a cylindrical sample about $8\frac{1}{4}$ in. long.

$$M = (0.5 \text{ Li}^+, 0.5 \text{ Fe}^{3+})$$

Magnetomechanical ratios g' were measured at $(295 \pm 2)^\circ\text{K}$ on seven different ferrites in the lithium series with the results shown in Table I. In these ferrites, Fe^{3+} is the only magnetic ion involved. Although the values of g' are all close to 2, there is (except for $x = 0.65$) a very definite trend toward lower g' values for higher values of x .

In this ferrite series it is known that Zn^{2+} always occupies a tetrahedral (A) position and Li^+ an octahedral (B) position in the spinel structure.^{3,4} A formula for this series can therefore be written as



Using this ionic distribution, we have accounted for the saturation magnetization values appearing in the literature⁵ by assuming a Yaffet-Kittel (YK) structure in which the B site Fe^{3+} ions are arranged in two sublattices having magnetizations directed at an angle α_{YK} to their resultant magnetization which is in turn antiparallel to a single A -site configuration as is apparently the case for the NiZn series.⁶ With $5\mu_B$ for Fe^{3+} , the expression for the resultant magnetization for this model would be

$$M = 5(1.5 + 0.5x) \cos \alpha_{\text{YK}} - 5(1 - x).$$

$\cos \alpha_{\text{YK}}$ was calculated from this expression for each value of x using values of M from Ref. 5.

If we now speculate that the g' values for Fe^{3+} ions on the sublattices are dependent on the value of the YK angle and have the spin-only value of 2.000 for $\alpha_{\text{YK}} = 0$, we can compute values of g'_B using our measured values of g' effective. Table

TABLE I. g' measurements for the ferrite series $\text{Zn}_x\text{Li}_{0.5-0.5x}\text{Fe}_{2.5-0.5x}\text{O}_4$.

x	g'
0.00	2.005 ± 0.002
0.50	1.998 ± 0.002
0.60	1.994 ± 0.003
0.625	1.989 ± 0.003
0.65	2.000 ± 0.002
0.70	1.982 ± 0.005
0.75	1.964 anomalous at room temp. (measured below 20°C)